Characterization of InAs-Al semiconductor-superconductor hybrid devices

Markus Aspegren

A Thesis Submitted for the Degree of Master of Science
30 credits
Supervisor: Assoc. Prof. Claes Thelander
Co-supervisor: Ph.D Heidi Potts

LUNDS UNIVERSITET

Division of Solid State Physics
Lund University
Sweden
May 2020

Acknowledgements

I would like to thank my supervisor Claes Thelander for his patience, and for telling me I was doing a good job even when I was not. His teachings, and teaching philosophy, is something I will bring with me in life. An example of a great tutor! I would also like to thank my co-supervisor, Heidi Potts, for always asking just the right questions to show that I had seldom read the articles as well as I thought I had. A brilliant individual who could read me like an open book! A special thanks to all the wonderful students with whom I shared an office, perhaps in particular Simon Wozny, Nils Lamers and Harald Havir, with whom I could never share too many coffee breaks, we tried. All in all it was a highly educational and enjoyable experience, all thanks to each of you!

Abstract

In this thesis we study charge and spin transport through InAs-Al nanowire superconductor-semiconductor hybrid devices. We focus on assessing the quality of the InAs-Al contact interface when using a weak HCl acid to wet-etch the nanowire surface prior to metal evaporation. The contact quality assessment is based on parameters extracted via electrical characterization performed mK temperatures in a dilution refrigerator. In order to successfully study transport through superconductor-semiconductor hybrids it is highly important to achieve a high-quality contact interface. With an ultimate goal of producing devices suitable for the study of hybridized sub-gap states in mind, we discuss the viability of using our proposed fabrication scheme in this context.

In hybrid devices there is superconductivity induced in the semiconductor via the proximity effect. The interplay between s-wave superconductivity from the superconductor and the unique properties of the semiconductor, e.g spin-orbit interaction, g^* factor, and tunable electron configuration via external gates, can give rise to exotic superconducting phenomena. Of particular relevance are Majorana bound states, which are candidates for the realization of stable qubits to be used in topological quantum computing. Experimental signatures of Majorana bound states have been reported in devices which are similar to devices presented in this thesis. This thesis attempts to further the understanding of quantum transport through, and in particular the magnetic field behavior of, proximitized nanowire quantum dots. Furthering this understanding proves beneficial when ultimately interpreting transport data in devices which are designed to hold Majorana bound states.

High-quality Al contacts on InAs nanowires have been manufactured and measured at mK temperatures. Supercurrents were measured in shunted Al-InAs-Al Josephson junction devices, and the critical magnetic field of the contacts was observed to depend on field direction. Excess currents were extracted in order to estimate the transparency of the contacts. Spectroscopy devices were manufactured study the density of states in a proximitized InAs segment in Al-InAs-Au nanowire-based devices, where a crystal-phase engineered band-offset has been incorporated in the semiconductor junction. These latter devices showed quantum dot behavior and a wide variation in coupling strength to the superconducting lead. We conclude the relative coupling strength primarily from observed degree of Yu-Shiba-Rusinov screening of dot spins, which determines the nature of our observed sub-gap states.

List of abbreviations.

YSR - Yu-Shiba-Rusinov
N - Normal
S - Superconductor
QD - Quantum dot
InAs - Indium arsenide
Al - Aluminum
ZB - Zincblende
WZ - Wurtzite
BCS - Bardeen–Cooper–Schrieffer
DOS - Density of states
MAR - Multiple Andreev reflection
DC - Direct current
AC - Alternating current
RCSJ - Resistively and Capacitively Shunted Junction
Ti - Titanium
SEM - Scanning electron microscope
HCl - Hydrogen chloride

Contents

1 Introduction

The phenomenon where the resistivity of a material drops to zero and shows a complete repulsion of magnetic fields when cooled to very low temperatures is known as superconductivity. The zero resistivity is essential for the strong magnets used in e.g particle accelerators or in nuclear magnetic resonance devices in hospitals. The magnetic field repulsion allows for levitating magnets above superconductors, an essential component for high-speed maglev (derived from magnetic levitation) trains in the future. Considering superconductivity in significantly smaller devices, a few microns in size, we find e.g the best magnetosensors in the world in the form of the superconducting quantum interference devices. Following the tremendous efforts over the past decades, which has led to a reduction of electronic components to the nanoscale, hybrid superconductor-semiconductor devices are now actively realized and this is an active research field. A major goal within this field is to fabricate stable superconducting qubits for use in quantum computing.

A transparent interface between a normal material (N) and a superconductor (S) induces a superconductivity proximity effect in the normal material[1]. Cooper pairs in the superconductor do not just disappear at the S-N interface, but instead leak into the normal material, where they remain phase-coherent until being scattered. The proximity effect can drastically alter the electron transport properties of the normal material and even allow for dissipationless currents across sufficiently short junctions.

The possibility of inducing superconductivity effects in otherwise non-superconducting materials allow for the study of exotic superconducting phenomena. Of particular interest in this project are superconductor-semiconductor hybrid devices. These systems allow e.g spin-manipulation of Cooper pairs and spin-resolved spectroscopy of superconducting devices[2][3].

A significant portion of contemporary research in semiconductor-superconductor hybrids tend to focus on potential future uses in quantum computing. Experimental signatures of Majorana bound states have been found in one-dimensional superconductor-semiconductor hybrids, typically in the form of zero-bias conductance peaks in spectroscopy measurements at finite magnetic field. Majorana bound states have been proposed to form the basis for qubits to be used in topological quantum computing[4]. It has been proposed that devices with integrated quantum dot(s) can be used to do spectroscopy on Majorana bound states[3].

A superconductor has a gap in the density of states surrounding the Fermi energy. Coupling a superconductor to a semiconductor can result in an induced gap in the semiconductor via the superconductivity proximity effect. In recent years there has been an influx of articles published regarding spectroscopy on sub-gap states, e.g those resulting from Yu-Shiba-Rusinov (YSR) screening of dot spin states in superconductor-quantum dot (S-QD-N) devices[5]. As a direct extension to this, there have been S-QD-QD-N devices realized in order to study the YSR-screening of spin states in quantum dot molecules[6].

Devices studied in this project are nanowire InAs-Al semiconductor-superconductor hybrids. InAs is actively used in quantum transport experiments, owing to its high mobility electrons, large Landé g-factor, and large spin–orbit interaction. These features can lead to a comparatively long mean free path and excellent spin-manipulation via externally applied magnetic fields. In addition, InAs is prone to form Schottky-barrier free

semiconductor-metal interfaces, offering the prospect of highly transparent S-N contacts.

The goal of this thesis was to fabricate semiconductor-superconductor devices with high-quality superconducting contacts. This was done in two separate systems. Firstly, the quality of the contact interfaces was assessed from relevant parameters derived from measurements on supercurrents in S-InAs-S devices, based on pure zincblende (ZB) nanowires. There are ample of available literature on similar, Al-InAs-Al, devices to compare the contact quality interface to. Secondly, S-InAs-N devices were used to do spectroscopy on the density of states of the induced superconducting gap. A crystal-phase engineered band-offset was incorporated in the semiconductor junction of the spectroscopy devices. The conduction band of a wurtzite (WZ) segment is offset a ZB-segment by ≈ 95 meV[7]. The S-InAs-N devices behaved as S-QD-N devices with strong coupling to the superconducting lead, resulting in sub-gap states.

2 Superconductivity

Superconductivity is a thermodynamic phase which exists for some metals and compounds at low temperatures. The phase transition occurs as the temperature is lowered below the critical temperature T_c. Associated with phase transition is, in particular, two features that drastically alters the electronic transport properties of the material: perfect diamagnetism and the existence of a zero-resistance state. The first implies that the interior of a superconductor is completely shielded from external magnetic fields, while the second allows for dissipationless currents. Superconductivity was first observed by Heike Kamerlingh Onnes in 1911 during transport measurements on mercury cooled to sub 4K temperatures[8].

Following its discovery, there was no shortage of experiments probing superconducting phenomena. Spectroscopy experiments indicated the existence of an energy gap around the Fermi level, which also revealed itself via a drastically altered heat capacity as the temperature was lowered below T_c. The perfect diamagnetism revealed itself in measurements with applied magnetic fields and is known as the Meissner effect, and is particularly clear in measurements with a superconducting ring or when magnets levitate over superconductors. Combinations of these measurements revealed that the magnitude of the energy gap was related to temperature and applied magnetic fields, and measurements with isotopes of mercury showed a direct link between the size of the energy gap and the atomic mass of the lattice.

Theories describing and predicting parts of the experimental results emerged early on, e.g the London equations. However, it took several decades for the BCS-theory to emerge[9]. BCS was the first theory to directly link microscopic quantum effects and the macroscopic effects seen in superconductivity experiments and is treated in Section 2.1.

Further interesting properties of superconductors emerge when it is proximitizing a normal material. Superconductivity leaks across the superconductor-normal interface and alters the transport properties of the normal material. This phenomenon is commonly referred to as the proximity effect and is covered in greater detail in Section 2.2.

Going one step further and sandwiching a normal material between two superconductors one forms a Josephson junction, a most important component of the vast majority of superconductivity based devices. With ample interesting properties, physics and uses on their own a full sub-chapter is dedicated to them in Section 2.3.

Coupling a superconductor to states in quantum dots realizes sub-gap states. By weakly coupling a normal contact to a proximitized quantum dot, a S-QD-N system, it is possible to do spectroscopy on the density of states of the proximitized system. These hybrid S-QD-N devices are covered in Section 2.4

2.1 BCS-theory

This section covers a summary of key components of Bardeen–Cooper–Schrieffer (BCS) theory[9], which was the first model capable of describing macroscopic superconductor properties, starting from microscopic quantum mechanics. BCS-theory immediately explained the heat capacity of superconductors, the isotope effect, and the appearance of a gap in the density of states around the Fermi level, all of which had been observed in a multitude of experiments at the time. Most of the contents in this section follow what is presented in [10].

A cornerstone of BCS-theory is that electrons, mirrored in energy on the Fermi surface and with opposing spins can pair up to form Cooper pairs[11]. Cooper pairs are bosonic quasi-particles which follow Bose-Einstein statistics. This implicates the formation of a condensate at sufficiently low temperatures. The momentum state of these pairs can be thought of as $|-\mathbf{p_i}\uparrow, \mathbf{p_i}\downarrow\rangle$. Momentum changes from scattering events for individual electrons are compensated by the corresponding paired up electron. All Cooper pairs in the condensate have the same momentum, $|(-\mathbf{p_i}+\mathbf{P/2})\uparrow, (\mathbf{p_i}+\mathbf{P/2})\downarrow\rangle$, where $\mathbf{P}$ is the momentum of the Cooper pair. This allows the full superconducting state to be described by a macroscopic wave function

$$\Psi_P = \Psi \exp(i\phi), \tag{1}$$

where ϕ is the phase of the superconductor. From this one can deduce that a supercurrent will flow only if the superconductor phase varies in space.

The pair-up process result in an energy gap, void of unpaired electrons, whose magnitude is commonly denoted as 2Δ, where Δ is the minimum energy required to break a Cooper pair. A schematic of the superconducting gap is seen in Figure 1. The aforementioned energy gap formation is equivalent to a change in the density of states of the system with an energy gap 2Δ around the Fermi energy.

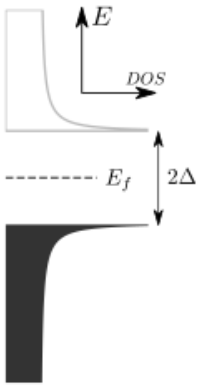

Figure 1: Schematic of the superconducting DOS, showing the energy gap of 2Δ.

The pairing of particles requires a net attractive interaction. The notion of two electrons, repelled by Coulomb interaction, ending up with a net attractive force is perhaps counter-intuitive. However, in metals charge screening results in a rapid reduction in repulsion from Coulomb interaction as a function of distance $|r - r_0|$. At separations

$|r - r_0| < T_f$, where T_f is the Thomas-Fermi screening length, the Coulomb interaction drops rapidly and is essentially non-existent in metals over distances of tens of nm. Meanwhile, long-range attractive forces between electrons can arise from electron-phonon-electron interaction in crystal lattices. The average separation between pairing electrons in the condensate is denoted as the coherence length ξ_0[9]. That superconductivity was closely related to lattice interaction had been known from experiments for a long time. Early experiments had found a direct link between the size of the superconducting gap and the isotopic mass of the lattice[12].

Returning to the discussion on the density of states of superconductors, we find that in the normal state the density of states (DOS) around the Fermi level, E_f, can be considered effectively constant across the range of Δ, which tends to be on the order of tens of µVe for Type I superconductors. Below the critical temperature, T_c, and the critical magnetic field, B_c, the material undergoes the superconductivity phase transition and the DOS changes to

$$N(E) = \begin{cases} 0 & \text{if E} < \Delta, \\ \dfrac{|E|}{\sqrt{E^2 - \Delta^2}} & \text{if E} > \Delta \end{cases} \tag{2}$$

which is in agreement with experiments using tunneling probe contacts[13].

With a finite Δ comes an upper limit on temperature, T_c. At temperatures $> T_c$ thermal excitations break Cooper pairs and destroy the condensate. BCS predict a relation between the size of the gap and T_c as:

$$\Delta(T = 0) = 1.764 k_B T_c \tag{3}$$

and a temperature dependence of Δ as:

$$\Delta(T) = \Delta(T = 0) \sqrt{\cos\left[\frac{\pi}{2}\left(\frac{T}{T_c}\right)^2\right]}. \tag{4}$$

Hence the energy gap shrinks with increasing temperature until it disappears at $T \approx T_c$. External magnetic fields quenches superconductivity both by increasing the kinetic energy of Cooper pairs, and by polarizing spins via the Zeeman effect. BCS theory predict that Δ depends on the applied magnetic field as

$$\Delta(B) = \Delta(0) \sqrt{1 - \left(\frac{B}{B_c}\right)^2}. \tag{5}$$

2.2 Proximity effect

This section discusses the physics related to the immediate proximity of a superconductor (S) and normal conductor (N) interface.

Cooper pairs in the superconductor do not disappear immediately at the S-N interface, but leak in to the normal material[1]. There the Cooper pairs remain paired up for a finite distance. This characteristic length is proportional to several material specific properties, primarily the coupling between the superconductor and the proximitized medium and the coherence length of the normal conduction barrier, ξ_n. A feature unique to semiconductor-superconductor hybrids is partial control of the phase-coherence length by tuning the electron population in the semiconductor[14].

Electron transport across S-N interfaces is dominated by Andreev reflections. Electrons approaching S from N travel as unpaired electrons which are strictly forbidden to enter the superconductor energy gap. Hence, electrons with energy $|E| < \Delta$ are either reflected by specular reflection, or pair up with an electron with opposing spin and energy and enter the superconductor as a Cooper pair. Left behind the pair-up process is a vacancy, i.e a hole, which retraces the path of the incident electron as a retro-reflected hole, see Figure 2a). An identical process occurs for holes approaching the superconductor, were they are instead retro-reflected as spin-flipped electrons, and a Cooper pair is removed from the superconductor condensate. Repeated Andreev processes are the origin of Andreev bound states for S-N-S structures in equilibrium, see Figure 2b).

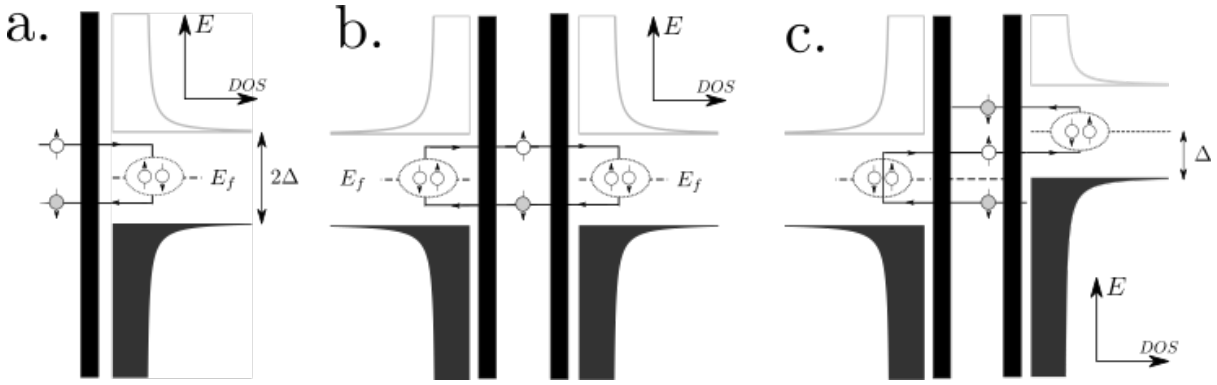

Figure 2: In a) schematic of the Andreev process. An electron/hole impeding the superconductor from the normal conductor, pairs up with an electron/hole with opposite spin and momentum and enters the superconductor as a Cooper pair. In b) resonant Andreev processes between two weakly coupled superconductors in equilibrium form Andreev bound states, allow dissipationless currents to flow through the junction. In c) a bias $V = \Delta/e$ is applied across the leads, leading to multiple Andreev reflections (MARs). In voltage driven Josephson junctions MARs appear as conduction peaks at integer fractions of 2Δ.

2.3 Josephson junctions

For two superconductors linked via a weak link the system is described by a uniform condensate wavefunction. Such junctions are referred to as Josephson junctions and are critical components of many superconductor based devices, e.g SQUIDs (superconductor quantum interference devices) which are highly sensitive magnetosensors[15]. A schematic

of a Josephson junction is seen in Figure 3. In our experiments we fabricated Josephson junctions where two superconductor leads are connected via an InAs nanowire. These superconductor leads consist of a 90 nm Al layer superposed on a 5 nm Ti layer.

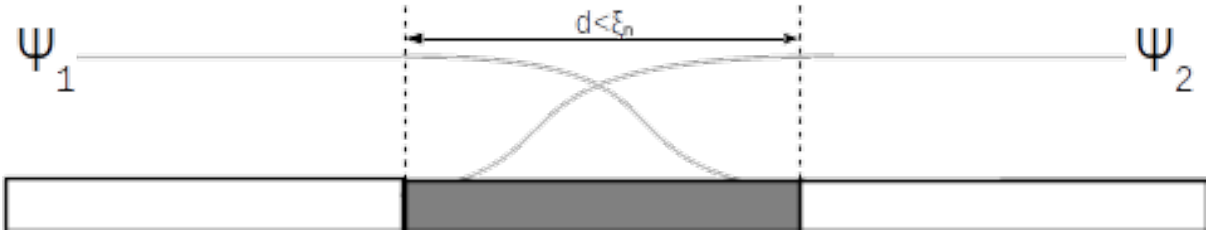

Figure 3: A schematic of a Josephson junction. The separation d denotes the length of a normal conducting material sandwiched between two superconducting leads, with superconductor order parameters Ψ_1 and Ψ_2, respectively. If d is less than the coherence length ξ_n of the normal conducting barrier the two leads are coupled via the normal conductor.

The phase of a quantum state lacks physical significance on its own. However, the phase difference of two interacting states can have meaning and is of the utmost significance in a Josephson junction. Next we present the relevant theory to understand the behavior of a Josephson junction when driven either by current or by voltage. These two cases yield very different outcomes in Josephson junctions.

Considering a Josephson junction with two superconducting leads, each in its own state (Ψ_1, Ψ_2) and with its own associated phase (ϕ_1, ϕ_2), the phase difference $\delta\phi = \phi_2 - \phi_1$ determines the current flow through the junction as

$$I = I_c \sin(\delta\phi) \tag{6}$$

where I_c is the critical current through the junction before the junction breaks down. This equation is known as the first Josephson equation. In equilibrium the current flow through the junction is constant, and for driven currents $I < I_c$ the phase difference $\delta\phi$ adjusts accordingly. When a current $I > I_c$ is driven through the junction the induced superconductivity breaks down. The phenomena of a dissipation-less current flowing through the junction, with zero applied bias, is known as the DC-Josephson effect.

The second Josephson equation is

$$\frac{\mathrm{d}\phi}{\mathrm{d}t} = \frac{2eU}{\hbar} \tag{7}$$

meaning that the phase difference across the junction varies linearly in time, at a frequency proportional to the bias applied. Inserting Equation 7 in Equation 6 we can deduce that an oscillation current with frequency $f = 2eU/h$ is to be expected for constant bias, a phenomenon known as the Josephson AC-effect. The radiation emitted from the AC current has been detected[16], but it is more common to perform the inverted experiment of applying radiation of relevant frequency, which results in the discretization of the Josephson current at steps of $2e/h$. These steps are known as Shapiro steps[17].

For a more complete picture of the $I - V$ characteristics of Josephson junction one must consider, in addition to the paired up electrons, the lead-lead capacitance as well as the normal conducting electrons. The contributions of these elements are included in

the Resistively and Capacitively Shunted Junction (RCSJ)-model. The relevant circuit diagram is shown in Figure 4.

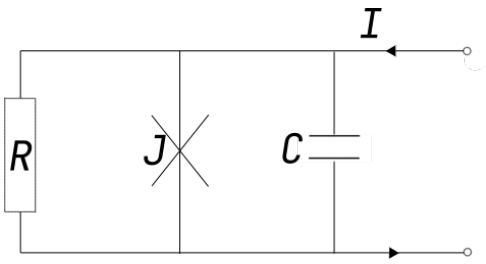

Figure 4: Schematic of the circuit considered within the RCSJ-model. In circuit diagrams a Josephson junction is commonly depicted with a cross (center). A load (left) arises from unpaired (normal) electrons not part of the superconducting condensate, while a finite capacitance (right) is commonly found between the two superconducting leads of a Josephson junction.

The total current I_{tot} is the sum through all three paths depicted in Figure 4. Hence

$$I_{tot} = I_c \sin\phi + \frac{U}{R_n} + C\frac{\mathrm{d}U}{\mathrm{d}t} \tag{8}$$

where U/R_n is the current contribution from normal electrons and $C\frac{\mathrm{d}U}{\mathrm{d}t}$ that of the lead-lead capacitance C.

Combining the second Josephson equation, Equation 7, with Equation 8 yields a non-linear differential equation for ϕ. Solving the resulting equation one has to distinguish between two limits with respect to the so called Stewart-McCumber parameter:

$$\beta_c = \frac{2e}{\hbar} I_c R_n^2 C \tag{9}$$

If $\beta_c >> 1$ there are two stable solutions, resulting in hysteresis in the $I-V$ characteristics with regard to the starting bias. Starting from $I > I_c$ the voltage drop across the junction does not drop to zero until the so-called retrapping current, I_R, is reached. If the sweep starts with $I \leq I_c$ the voltage drop across the junction remains zero until $I > I_c$. Hysteresis in the $I-V$ characteristics is the typical case for the devices presented in this thesis.

So far we largely covered Josephson junctions in equilibrium, see Figure 2 b). Considering the case where the junction is voltage-biased, see Figure 2 c), it is possible to see conduction peaks at $eV_{sd} = 2\Delta/(ne)$, where $n = 1, 2, 3...$[18]. The 2 originate from the fact that there are two superconductors, each with the superconducting order parameter Δ. These peaks arise due to MARs, see Figure 2c). Being a two particle process there is significant requirements on contact transparency for Andreev reflections, and parameters associated with Andreev reflections are often used to derive contact characteristics in Josephson junctions. This requirement also applies for MARs, and the number of discernible peaks are occasionally used as a semi-quantitative way to discuss the contact transparency.

2.4 Superconductor-quantum dot devices

Devices that have discernible energy quantization in all three dimensions are typically referred to as quantum dots (QD). At low enough temperatures the energy required to add an electron to the dot exceeds the thermal energy, which in combination with electrostatic control of the electrochemical potential of the dot via external electrode(s), allows for single-electron transistors[19]. We refer to Figure 5a-c) for schematics related to transport through a quantum dot. The total spin of the dot directly follows the electron occupation and typically varies between $s_z = 0$ for even number of electrons and $s_z = \pm\frac{1}{2}$ for an odd number of electrons.

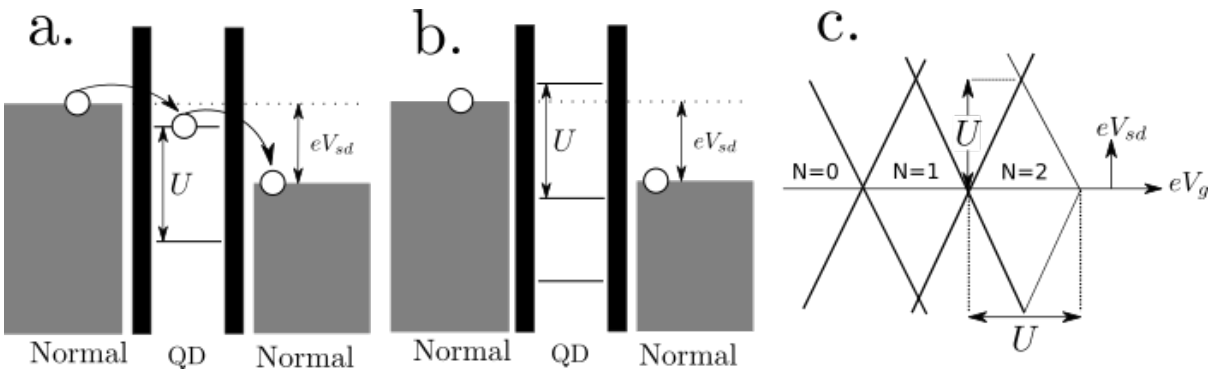

Figure 5: Transport through a quantum dot. In a) there is an available state inside the source-drain bias window V_{sd}, allowing electrons to tunnel through the dot one by one. In b) no such state is available inside the bias window, blocking charge transport through the dot. In c) a schematic of "Coulomb diamonds", where the Coulomb blockade phenomena depicted in b) result in diamond shapes while measuring current and sweeping both V_{sd} and V_g. The diamonds have height and width equal to the charging energy, U. This can be used to control the electron occupation of the quantum dot.

We now discuss charge-carrier transport through S-QD-S/N hybrid systems. Proximitizing levels in a quantum dot with superconductor lead(s) can result in hybridized sub-gap states. It costs the energy Δ to break a Cooper pair, while Coulomb repulsion only allow for one-by-one filling of electrons on the dot. The nature of the hybridized states is governed by the relative magnitude of the coupling strength to the superconducting lead, Γ_S, the size of the superconducting gap, Δ, and the dot charging energy U[20].

The coupling strength between lead- and dot states is primarily determined by the corresponding tunneling density of states. The devices considered in the following example have one normal and one superconducting lead, and the coupling strengths are denoted Γ_N and Γ_S, see Figure 6. The superconductor-quantum dot coupling can result in sub-gap states in S-QD devices, given sufficiently large Γ_S. For the following paragraphs we assume Γ_N to be weakly coupled, meaning that $\Gamma_N << \Gamma_S, \Delta, U$.

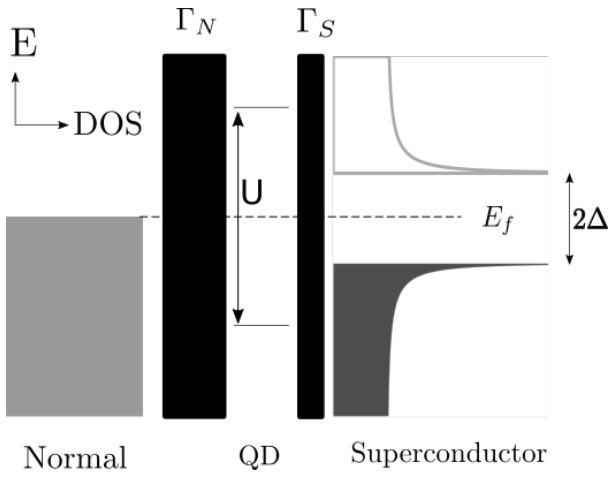

Figure 6: Schematic of a N-QD-S hybrid system with energies involved in the problem.

The lead coupling Γ_S sets the broadening of quantum resonant levels, see Figure 7. Increasing the ratio of Γ_S/Δ increases the correlation amplitude between electrons on the quantum dot with Bogoliubov quasiparticles above the superconducting gap. For large enough Γ_S/U the broadened levels can even cover the entire Coulomb blockade region, drastically increasing the amplitude higher-order tunneling events. These higher-order tunneling events are commonly referred to as cotunneling events as two or more electrons tunnel through simultaneously.

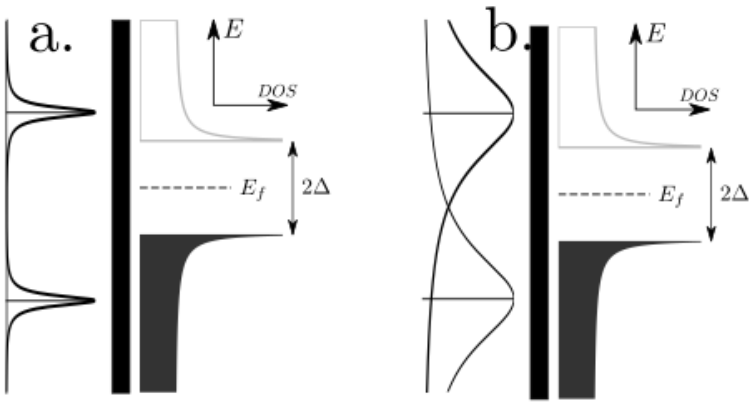

Figure 7: In a) reduced level broadening due to low Γ_S/U. In b): increased level broadening due to high Γ_S/U.

When $U << \Delta$, the energy required to break up Cooper pairs is significantly larger than the cost of adding electrons to the dot. Here we find that the dot can be driven superconducting via the proximity effect. The dot hybridizes with Cooper pairs, which allow Cooper pairs to tunnel in and out of the dot[21].

When $U >> \Delta$ the comparative cost of breaking a Cooper pair is low and the Bogoliubov quasiparticles, now close in energy, hybridize with the $|N = 1\rangle$ dot state. Andreev reflections are suppressed, while Bogoliubov quasiparticles with spin opposite the dot state are energetically favored. Hence, for any Γ_S bound states are formed between attracted Bogoliubov quasiparticles and odd-occupation dot states. For low Γ_S the bound

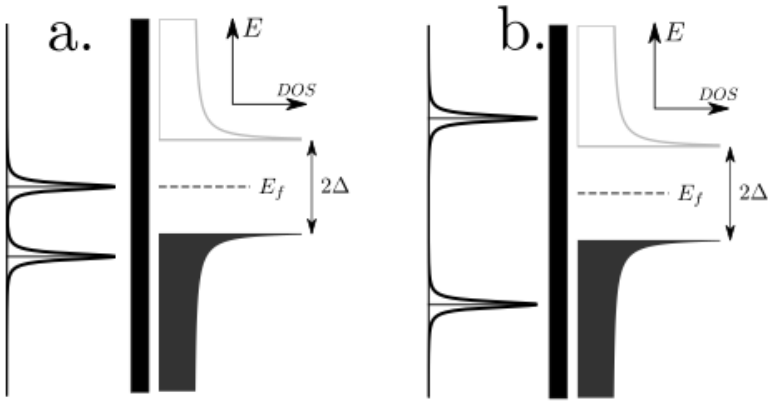

Figure 8: Left: Low U/Δ. Right: High U/Δ.

state is situated just below Δ. At this point we have a doublet ground state (from an odd dot charge state), but as Γ_S is increased the bound state moves down in energy towards the Fermi level. Eventually the state crosses the Fermi level and a Bogoliubov quasiparticle effectively becomes trapped on the dot, screening the dot spin and resulting in a singlet ground state. This picture is a simplified one, where we somewhat erroneously assume that only the lowest energy Bogoliubov quasiparticle contributes in the screening process. This simplified image breaks down for larger Γ_S[5]. Nevertheless, the phenomena where Bogoliubov quasiparticles screen a magnetic impurity (here this is the dot spin), is known as Yu-Shiba-Rusinov (YSR) screening. The singlet, composed of a dot electron with a Bogoliubov quasiparticle, is known as a YSR-singlet.

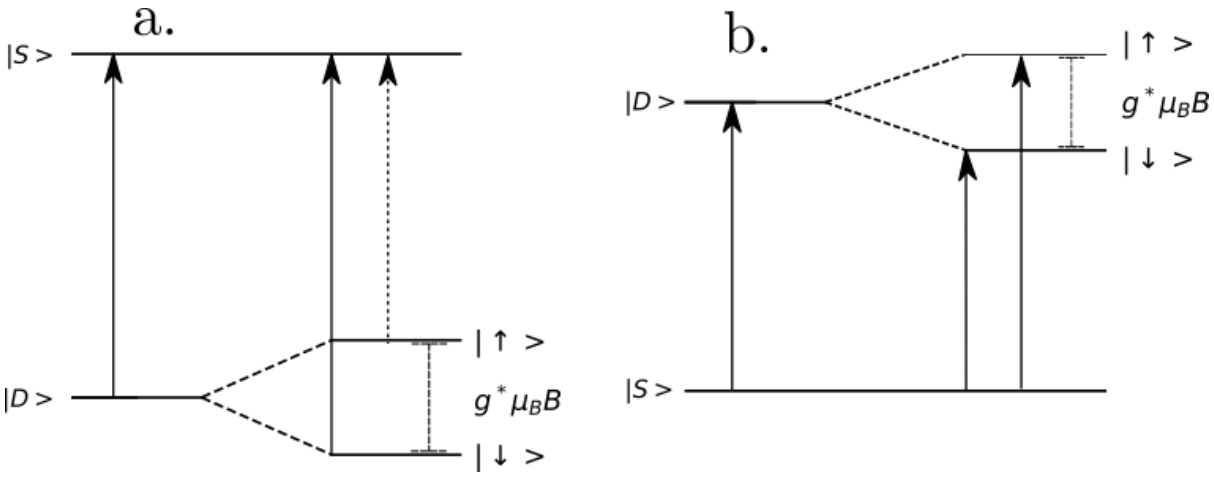

Figure 9: Visible excitation lines in spectroscopy measurements. Transitions marked with solid arrows have the largest spectral weight. In a) the doublet ground state has an excited singlet state. In b) the singlet ground state has a doublet excitation state.

Excitation lines which are typically seen in spectroscopy measurements on S-QD-N devices, assuming $\Delta << U$, are depicted schematically in Figure 9. Here an exciting possibility is implied for singlet ground states: what happens when B is large enough to push the $|\downarrow\rangle$ state *below* that of the singlet ground state? This implies a quantum phase transition, where ground state transitions from a singlet to a doublet via lifting the

spin-degeneracy. This phase transition can be observed in spectroscopy measurements via a crossing of the excitation lines as the ground state and excited state switch roles. This phase transition has been observed several times, e.g in references [5] and [20] .

3 Experimental details

All devices fabricated for this thesis are based on InAs nanowires and use Ti/Al (a 90 nm Al layer superposed on a 5 nm Ti layer) for superconducting (S) leads, and Ti/Au (a 70 nm Au layer superposed on a 5 nm Ti layer) for normal (N) leads. The wires have been deposited on a silicon substrate, which is glued onto a bond-chip using a micromanipulator. The silicon substrate separates the wires from a global back-gate on a bond-chip. The bond-chip is used to connect the fabricated nanoscale devices to the macroscopic electronics used for electrical characterization.

3.1 Fabrication

We fabricated S-InAs-S devices with a four-terminal design. These devices were designed to operate as Josephson junctions, and pure InAs ZB segments were used for the junctions. We also fabricated S-InAs-N devices with a two-terminal design. The latter devices were designed for spectroscopy measurements on the density of states on proximitized InAs segments. In these latter devices, we used InAs nanowires where the crystal phase was varied from WZ to ZB during growth, and the Ti/Al and Ti/Au contacts were deposited on opposite sides of the WZ-ZB interface. The protocols for each unique fabrication step were identical for both the S-InAs-S and S-InAs-N devices, but with some of the steps repeated for the S-InAs-N devices.

What follows are summaries of each fabrication step, which will be enumerated for easy referencing. The term 'sample' will refer to a chip at the relevant fabrication step, and on each sample there will be several devices. The chip is composed of a 200 nm thick SiO_2 insulator and a highly conductive layer of Si underneath. A chip is then glued to a chip carrier, between which bond-wires are formed.

After nanowire deposition, a scanning electron microscope (SEM) was used to take micrographs showing the location of nanowire candidates in relation to bond-chip markers (Step 1). These micrographs were used for contact design (Step 1.1). The sample was then covered in a positive electroresist (PMMA 950) via spin-coating techniques, where a revolutions-per-minute of 5000 was used for a duration of 40 s. Directly after spin-coating the sample was baked on a hot plate at 180°C for 5 min (Step 2). Electron-beam lithography was used to expose the resist according to the contact designs (Step 3). The resist was then developed using a mixture of methyl-isobutyl-ketone (MIBK) and isopropanole (IPA) (Step 4). To remove resist residue from the exposed nanowire segments the sample was plasma-ashed for 20 s (Step 5). To remove native oxides from the exposed nanowire segments the samples were wet-etched for 15 s in diluted HCl (1:20 by volume), and then submerged in diluted water and agitated for 20 s to wash away the HCl, followed by a short blow drying from a nitrogen gun (Step 6). Post HCl-etching the sample was moved into an electron-beam evaporator. The relevant metals (Ti/Al or Ti/Au) was deposited on the sample using electron beam evaporation (Step 7). In the final fabrication step the excess metal was lifted off by dissolving the underlying resist in a 65°C acetone bath (Step 8). When the lift-off procedure was complete the chemical process was terminated by washing the sample with IPA and the sample dried with a nitrogen gun.

For the Josephson junction devices (S-InAs-S) steps 1-8 were run once, with Ti/Al

used in step 7. For the spectroscopy (S-InAs-N) devices steps numbered 2 to 8 were repeated for each contact, with the Ti/Au contacts deposited on the first iteration and Ti/Al contacts the second.

Estimated average duration of air exposure during step 7 is on the order of 2 min, counting from the end of the wet-etching procedure in step 6, to initiating vacuum pumping of the evaporation chamber. Post contact deposition the samples were exposed to air multiple times during bonding procedures, some of our devices were exposed for hours during this phase.

3.2 Experiment setup

All measurements were done in a dilution refrigerator with a base temperature of ≈17 mK. At this temperature both elements in our Ti/Al contacts are superconducting. We use two different driving biases, current and voltage. These are swept as a function of backgate and magnetic field. Relevant concepts and schematics to the experimental setup are covered in the following paragraphs.

Vector magnet. To test the critical magnetic fields of our devices a vector magnet was used to apply magnetic field along different directions. The contacts vary in dimension, and the critical field of superconductor depends on the superconductor dimensions. In general: the smaller the field cross-section, the larger the critical field. Our contacts vary in size, depending on viewing angle. Hence, the critical field is expected to depend on direction. For our Josephson junction devices we chose to apply the field in three separate directions, these are depicted in Figure 10. The directions are: 1) perpendicular to the nanowire stem and aimed straight into the substrate surface, denoted $B_{\otimes}$, 2) perpendicular to the nanowire stem and parallel to the substrate surface, denoted $B_{\perp}$ and 3) parallel to both nanowire stem and substrate surface, denoted $B_{\parallel}$.

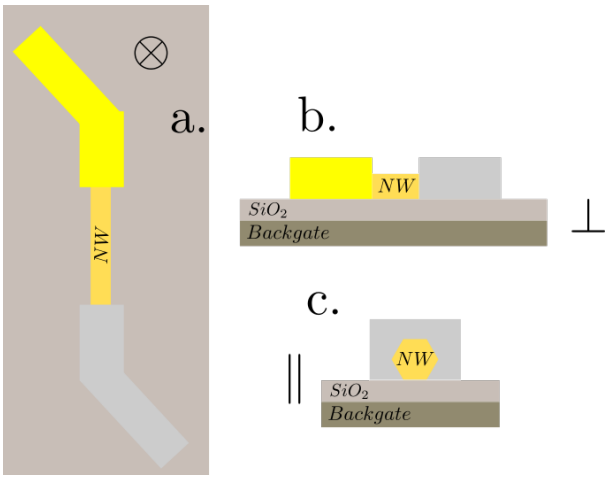

Figure 10: Schematic showing directions of applied magnetic field. In a) the field is perpendicular to substrate surface and nanowire growth direction, denoted ⊗. In b) the field is parallel to the substrate surface and perpendicular to nanowire growth direction, denoted ⊥. In c) the field is parallel to both substrate surface and nanowire growth, denoted ∥.

Current drive. To measure supercurrents through Ti/Al-InAs-Ti/Al devices a four terminal geometry was used, and a schematic showing important circuit components can

be seen in Figure 11a). The InAs segment situated between two leads, labeled source and drain respectively, is what is referred to by 'junction'. Here the goal is to drive a current through the junction while keeping the source-drain leads in equilibrium. This was possible by using a large resistance load, 1MΩ, in series with a voltage source. As the resistance of the devices was significantly smaller than the resistance of the external circuit the voltage drop over the devices is negligible. Between the 1MΩ resistor and the source lead a current amplifier was used. Post the drain lead we used a current-to-voltage converter. Simultaneously the voltage drop over the junction was measured via the two remaining terminals, connected in parallel over the source-drain leads.

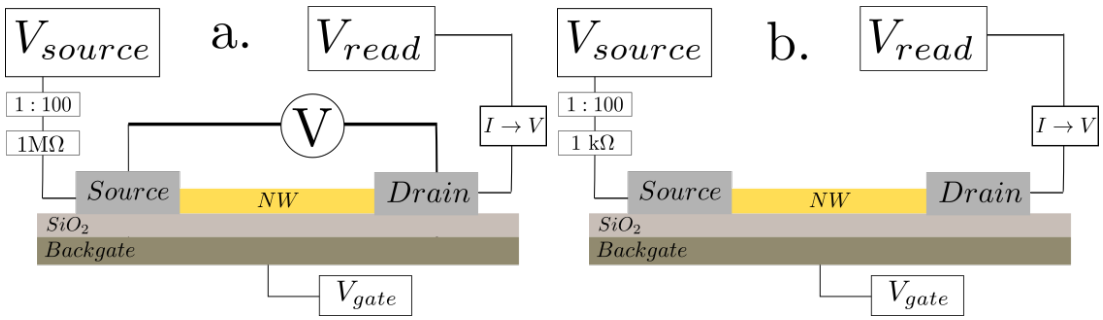

Figure 11: In a) schematic of measured devices and relevant electronics used for measurements with current drive. In b) the corresponding for voltage driven measurements

Voltage drive. This was the most commonly used experimental setup for experiments in this project. For the voltage driven experiments a two terminal geometry was used. A voltage source in series with a 1:100 voltage divider, a small load, R_L, is used to drive the source-drain leads out of equilibrium. Post the drain lead we used a current-to-voltage converter. For this setup the resistance of the external circuit is in general comparable to the resistance of our devices. This causes the size of the apparent gap to change with the conductance of our devices, which in particular fluctuates with V_g.

4 Results

4.1 Josephson junctions

This section covers the results of transport measurements on two Josephson junction devices, which differ only in the junction length. Both of the devices are seen in Figure 12, where the four-probe geometry can be seen. With values extracted from the SEM images, the junction length of device 1A is 150±5 nm while that of device 1B is 320±5 nm.

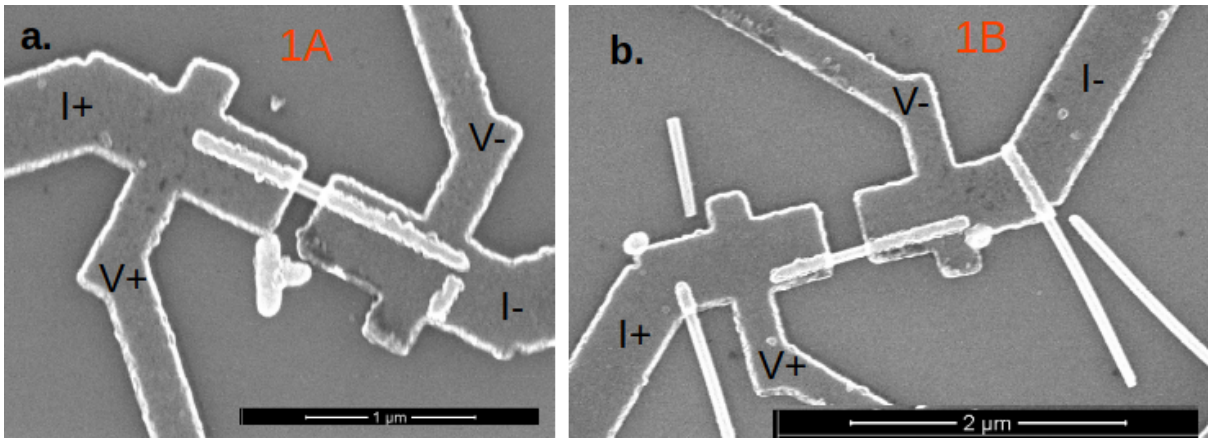

Figure 12: SEM micrographs of two Josephson junction devices. Both devices use a four-probe geometry. Ti/Al contacts have been deposited on InAs nanowires. Left is "device 1A", with a junction length of 150±5 nm. Right is "device 1B", with a junction length of 320±5 nm.

The primary goal of the experiments presented here was to extract and quantify parameters relevant to contact characterization of the Al leads connected directly to InAs nanowires. In relevant literature (eg. references [14, 22, 23, 24]) the critical current, I_c, the excess current I_{exc} and the size of the induced gap, Δ^* all have been used to assess the quality of the contact interfaces and Josephson junctions in similar devices, with varying degrees of success. A final parameter deemed interesting for contact characterization was the critical magnetic field, B_c. All parameters extracted from the measurements using a voltage drive have been corrected for the series resistance of the circuit.

Device 1B allowed for excellent tunability of I_c with gate bias. This is seen in Figure 13, where the $V(I)$-characteristics of device 1B are plotted for varying gate bias. A clear hysteretic behavior is seen, a common phenomenon in capacitively shunted Josephson junctions. Relevant theory is covered in Section 2.3. Likely the shunted behavior primarily originates via capacitive coupling to the back gate, rather than to source-drain leads. Had the capacitive coupling to the source-drain leads dominated one would expect 1A to show increased shunted behavior compared to 1B, due to the significantly shorter separation between contacts of 1B. The shunting behavior of both 1A and 1b is seen in Figure 14. Across the back gate range -5 to +10 V, values of I_c ranges between 0.8 and 5 nA. Denoting the normal state resistance of the junction as R_N, we find values of the I_cR_N product between 7-9 µV, indicative that the junction is long compared to the mean free path in the wire. Similar values of the I_cR_N product are seen for device 1A, which is kept at a nearly constant 8 µV, independent of gate bias in the range of -5 to +5 V.

As a comparison, a device operating in the ballistic limit may reach values comparable to Δ^* [25].

The similar values of the I_cR_N product of the two devices are unexpected. In [26] a strong link was found between the length of the junction and the value of the I_cR_N product, and the junction lengths of the two devices presented here differ by effectively a factor of two. Hence I_cR_N ought to be noticeably larger for device 1A than 1B, all other things equal. Such a scenario immediately brings to question if 1A has low transparency contacts, which could explain why the I_cR_N product would be lowered for 1A. Unfortunately, the device design did not allow for measuring contact resistance directly. However, given some comparatively very low values of $R_N = 600\ \Omega$ of 1A it is highly improbable to be low transparency contacts at play. The exact cause of why 1A has high or 1B has low I_cR_N will not be discussed further in this thesis given its low impact on the remainder of the work and goals of this project.

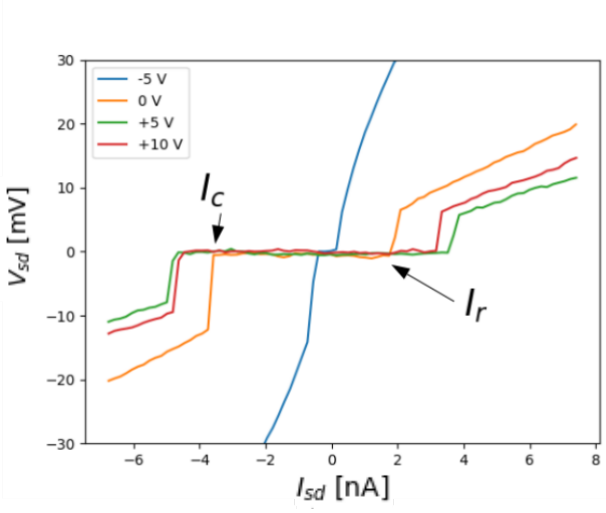

Figure 13: $V(I)$-characteristics of device 1B as a function of back gate. Sweeps are right to left. The critical- and retrapping current at 0 gate bias is marked with arrows.

In Figure 14 the differential resistance $\mathrm{d}V_{sd}/\mathrm{d}I$ of both devices is plotted as a function of the applied magnetic field in three different directions. The devices were current biased, and the voltage drop over the wire was measured via the four-point geometry. The largest critical- and re-trapping- Josephson currents are found at $B = 0$ for all field directions. As the magnetic field magnitude is increased the current magnitudes decrease until the device is driven normal at $B > B_c$. The decrease in critical current with the applied field is largely parabolic, as seen by the guided curve. This indicates that the reduction in critical current with the increasing field has to be associated with effects beyond solely the reduction of the gap. It is not straightforward to pinpoint B_c for any field direction due to the existence of the tail-like feature seen for all devices and field directions. The tail is possibly due to pockets of superconductor material which prove difficult to drive normal, as their small size leads to a larger B_c. The Al ends up forming small islands on the InAs surface with the used evaporation techniques, as can be seen quite clearly for device 1A in Figure 12. Another possibility is that the Ti component of the Ti/Al leads (Ti is also superconducting at the relevant temperatures) has a slighter larger critical field

than Al at the relevant contact dimensions. The relation between the field orientations is clear, with $B_{\otimes,c} \approx 45$, $B_{\perp,c} \approx 55$ mT and $B_{\parallel,c} \approx 90$ mT for the two devices.

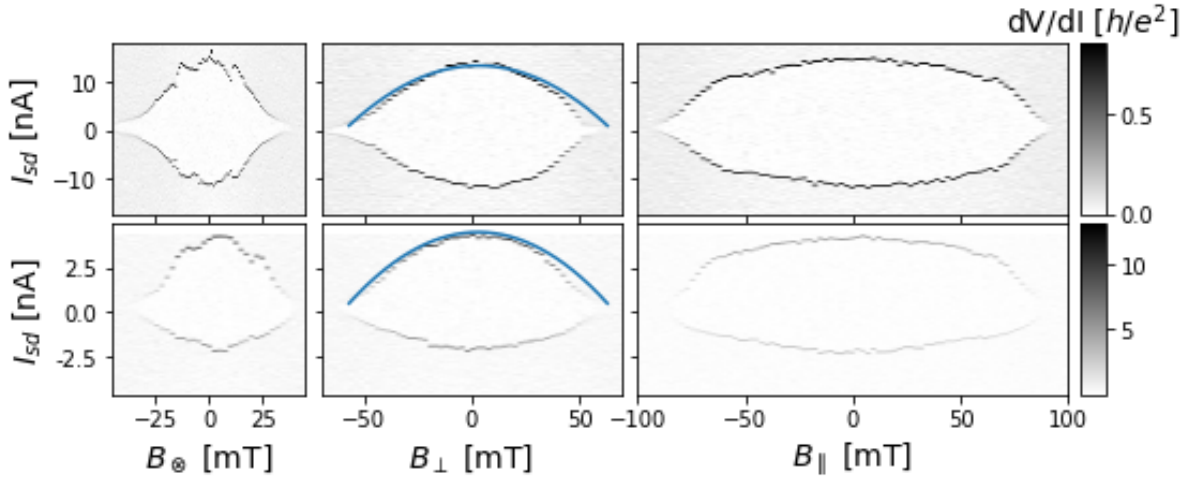

Figure 14: Differential resistance, dV/dI, of Josephson junction devices as a function of applied magnetic field in three separate directions, $B_\oplus$, $B_\parallel$, $B_\perp$. All sweeps are from negative to positive current bias, hence the retrapping current is found when the resistance drops to zero, starting from the bottom. The top row is device 1A, while the bottom row is device 1B. Note how B_c depends on field direction, and that the relative difference between retrapping and critical currents is significantly larger for device 1B than for 1A. For all plots, the gate bias is set to zero. Included in the $B_\perp$-plots are guiding lines showing $I_c/B_\perp^2$, slightly offset in I_c.

In Figure 15 the $\mathrm{d}I/\mathrm{d}V_{sd}$ of a voltage-driven Josephson junction is shown as a function of V_g. The applied V_g range is negative, causing significant electron depletion in the nanowire at the lower gate biases. While sweeping V_g an alternating on-off behavior is seen both for the device in a superconducting state and when it is driven normal by an externally applied magnetic field $B_\otimes$. Fluctuations in the superconducting peak (at zero bias) magnitude, ranging from highly suppressed when R_N is large to a conductivity peak when R_N is small, occurs at similar gate-bias. Similar on-off and transistor-like, behavior is seen in references [24, 27, 28]. The checkerboard pattern is seen in the normal state, highly prominent between -6.2 and -6 V, is indicative Fabry-Perot interference. A similar checkerboard pattern can be seen in e.g [28].

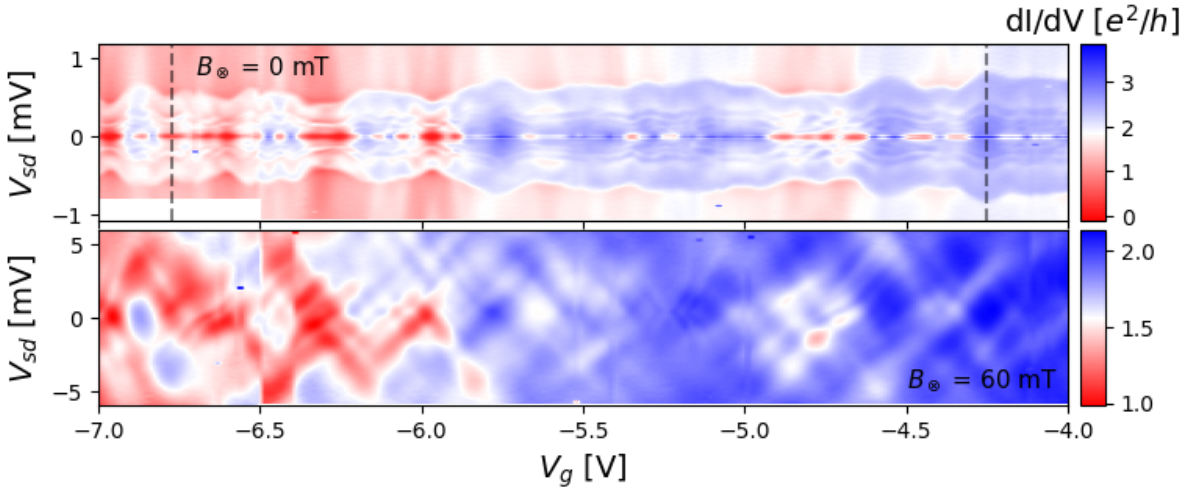

Figure 15: Differential conductance, $\mathrm{d}I/\mathrm{d}V_{sd}$, of a voltage-driven Josephson junction as a function applied back-gate. Top: device 1B in a superconducting state. Conduction peaks owing to Andreev reflections are seen at all gate-biases. Bottom: device 1B when driven normal by $B_\otimes$ = 60 mT. Note how the on-off behavior of the superconducting peak (at V_{sd}) state strongly follows the conductivity variations in the normal state.

Small discrete jumps are seen in the normal state, which is attributed to changes in electrochemical potential in the wire due to e.g releasing of trapped surface electrons, causing the perturbations seen at e.g $V_g = -6.5$ V.

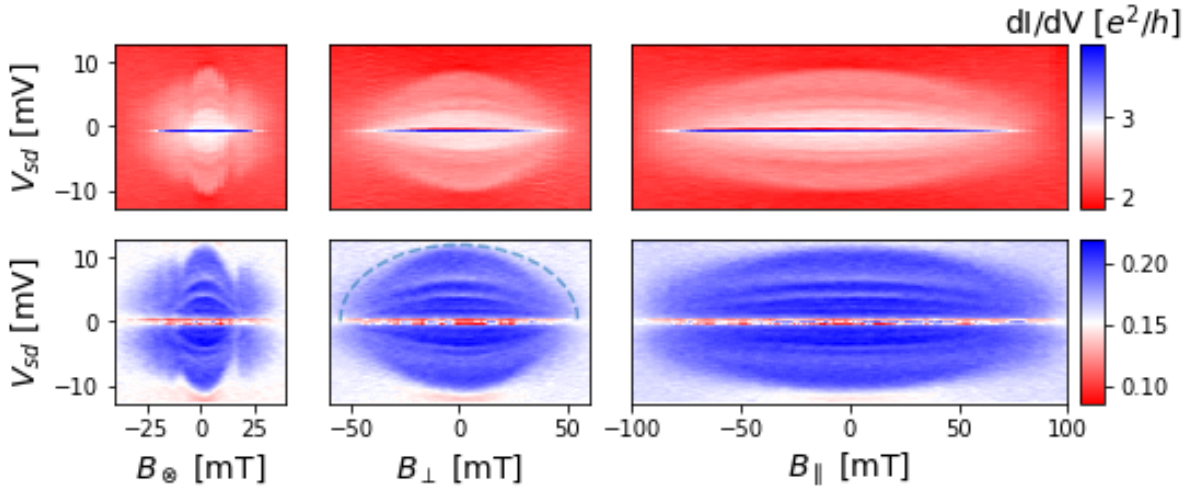

Figure 16: Differential conductance, $\mathrm{d}I/\mathrm{d}V_{sd}$, of device 1B as a function of applied magnetic field in three separate directions. Top row: B-field sweeps along the on-state marked with a dashed line at V_g =-4.25 V in Figure 15. Bottom row: back gate set at the off-state at -6.775 V, also marked in Figure 15. We define off-states as regimes where the superconducting peak is strongly suppressed, which is indicated by the scale. In all plots conduction peaks resulting from Andreev reflections are seen.

In Figure 16 the on- and off-states marked with dashed lines in Figure 15 are probed in greater detail. The $\mathrm{d}I/\mathrm{d}V_{sd}$ is shown as a function of applied magnetic field. A strong

characteristic of voltage-driven Josephson junctions is the zero-bias superconducting peak, which is clearly seen in the on state. The off-state also show a superconducting peak, albeit strongly suppressed, which is easier to see in Figure 17a). The critical fields are much easier to extract here as compared to the previous I_c case, and as indicated by the fit of $2\Delta(B)$ (Equation 5) at $B_\perp$ in the off-state we now directly see the reduction in Δ with applied field. $B_\otimes$ still has its peculiar features, and these are still hypothesized to originate from superconducting pockets forming on the InAs surface. We find $B_{\perp,c} \approx 55$ mT, $B_{\parallel,c} \approx 95$ mT. In both the on- and off-state several MARs are visible at energies $2\Delta, \Delta, 2\Delta/3$.., and are seen slightly clearer in the lineplots presented in Figure 17.

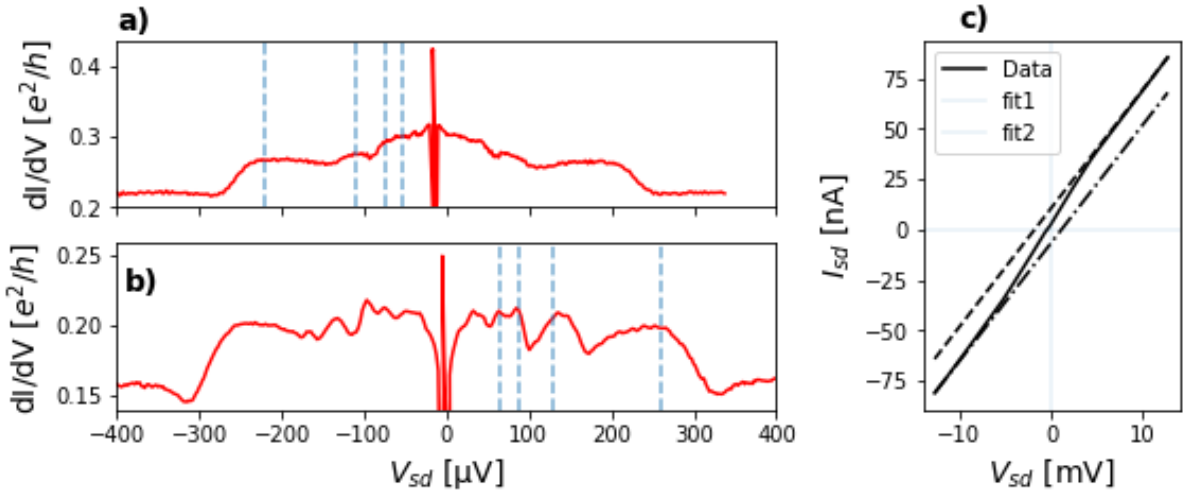

Figure 17: Differential conductance of device 1B at $V_g = -4.25$ V (a) and $V_g = -6.775$ V (b). Several MARs are seen both in the on- and off-state, marked with dashed lines. In c) method of extracting I_{exc} from data. Extrapolating the current at $V >> \Delta$ to $V = 0$ in a voltage driven Josephson junction, and taking the difference to the measured current at $V = 0$ one finds I_{exc}.

Now we move onto the final parameter of interest, the excess current. We refer to Figure 17b), which aids in the understanding of the definition of the excess current. Extrapolating the current from $V_{sd} >> \Delta$ to $V_{sd} = 0$ the excess current is defined as the difference between the extrapolated current and $I(V_{sd} = 0)$. From the data presented in Figure 15 a wide range of I_{exc} is derived, from 0 in the off-states to $\approx$ 22 nA in the on-states. Along with values of R_N from the normal-state data in Figure 15 and using an average value of $\Delta^* = 120$ µV, the final, unitless, $I_{exc}R_N/\Delta$ product could be derived across the range -7 to -4 V. Across this range values of $I_{exc}R_N/\Delta$ range from 0 in the off-states, up to ≈ 2 in the on-states. The larger value is a rather exciting result, indicative of very transparent contacts. See Figure 18 for typical barrier strength to $I_{exc}R_N/\Delta$ product relations.

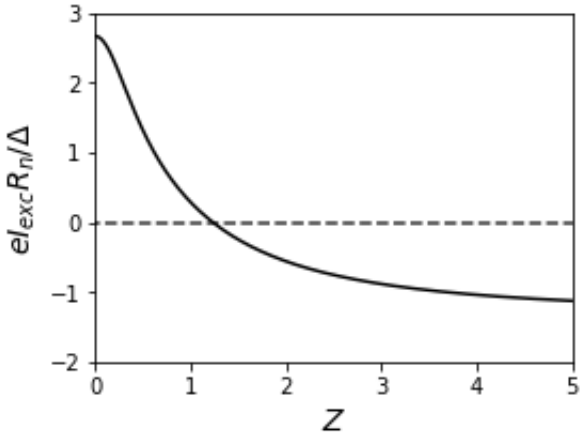

Figure 18: Relation between $I_{exc}R_N/\Delta$ to barrier strength Z, where Z is related to barrier transparency, T via $T = 1/(1 + Z^2)$. Adapted from [29]

Typically the $I_{exc}R_N/\Delta$ product is used to make estimates on the barrier across the junction, including both contacts and the normal conductor itself. By deriving the $I_{exc}R_N/\Delta$ product across a wide range of V_g, and making the assumption that the contact transparency is largely unaffected by a change in gate bias, we can reason that the largest changes in the $I_{exc}R_N/\Delta$ product originate from changes in R_N. For the largest $I_{exc}R_N/\Delta \approx 2.5$ product we find the lowest barrier strength $Z = 0.3$. In turn Z is used to extract an upper value for the transparency through $T = 1/(1 + Z^2)$, giving $T = 91\%$.

4.2 Spectroscopy on Al-InAs-Au devices

The initial goal of the experiments presented in this section was to do spectroscopy on the density of states in a proximitized InAs segment, and investigate how the inclusion of a ZB-WZ interface in the junction affects the measurement. In total three devices were studied at mK temperatures, two of these have Al-WZ-ZB-Au configuration and one has a Au-WZ-ZB-Al configuration. All three devices showed quantum dot behavior, and each device with its own unique set of Γ_S, Γ_N and U. Each of these parameters also varied with the electrostatic potential of the dot, offering a very interesting opportunity to study a wide range of hybridized sub-gap states. Making stability diagrams in a larger V_{sd} range proved difficult for all devices, significant line broadening made it in general impossible to see the Coulomb diamonds. Likely the cause of this complication is tunnel broadening from both leads. The devices and results of spectroscopy measurements for each device will be presented one by one, starting with the two Al-WZ-ZB-Au devices.

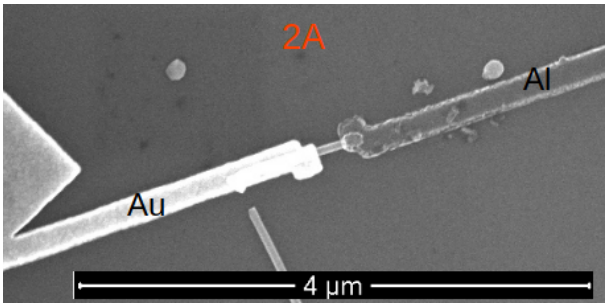

Figure 19: SEM micrograph of device 2A.

The first device to be covered is seen in Figure 19, where a SEM image of the device is shown. Two probes are used, one superconducting (Ti/Al) on the WZ segment and one normal (Ti/Au) on the ZB segment. The electrochemical potential of the dot could be controlled, and there were no complications when tuning the electron occupation on the dot.

The transport characteristics of a region close to V_g=+4.4 V is seen in in Figure 20. It shows the differential conductance, $\mathrm{d}I/\mathrm{d}V_{sd}$, across a few dot orbitals and as a function of a magnetic field applied along the wire. The superconducting gap shows itself clearly in this plot, and while it always shrinks with increasing magnetic field, it seems to do so at different speeds for the different orbitals. The orbitals marked I-III show tendencies of $\Gamma_S << U$, as no distinction can be made between odd-even occupation numbers even with an applied magnetic field, which implies that we are far from a YSR-regime. Instead, this regime is likely to have proximity induced sub-gap states, where states consist of a Cooper pair and a superposition of $|N = 0\rangle$ and $|N = 2\rangle$. This changes at the orbital marked IV, something drastic happens as the gate bias is increased, and Γ_S increases enough to induce a YSR-state. The drastic increase of Γ_S coincides with a visible sharp feature, which might be from an additional dot in the system. As the applied magnetic field increases the excited doublet state begins to split. The g^*-factor varies across orbital IV, and where it can be extracted we find values between 3-5, with the larger values found where the excited state is far from the gap.

Another hot topic in research surrounding superconductor-semiconductor hybrid devices is the hardness of the induced gap. Unlike the superconductor gap, where the density of states below $|\Delta|$ is strictly zero, the density of states of the induced gap inside the semiconductor is not strictly zero for $E < |\Delta^*|$[30]. The fewer available states inside the induced gap, the harder the gap. A way to quantify this to compare the suppression factor of G_S/G_N, where G_S is the conductivity inside the gap and G_N the conductivity a distance away from the gap. The larger the suppression factor, the harder the gap. This was done along the dashed line in Figure 20, and is presented in Figure 20 b). Here the gap shrinks with increasing magnetic field, but the suppression factor remains large until the gap is nearly closed at 120 mT. The suppression factor found for zero magnetic field is ≈40, which is a comparatively large suppression factor considering the simplicity of the processing protocols for these devices. As a comparison: suppression factors of around 100 were found in [30] where, in contrast, some very specialized fabrication protocols were used.

Along the same dashed line in Figure 20a) the critical magnetic field $B_{\parallel,c}$ was tested and found to be ≈140 mT. This is significantly larger than what was found in Section 4.1

for the Josephson junction devices, where $B_{\parallel,c}$ was below 100 mT. This is very positive in the sense that a larger critical magnetic field is highly useful here, but can be slightly problematic in the sense of reproducibility. The contacts were not designed to be identical to those of the Josephson junctions, so perhaps reproducibility is not really an issue, but rather a positive indication that the magnitude of the critical magnetic field can be greatly enhanced with minor changes in contact design.

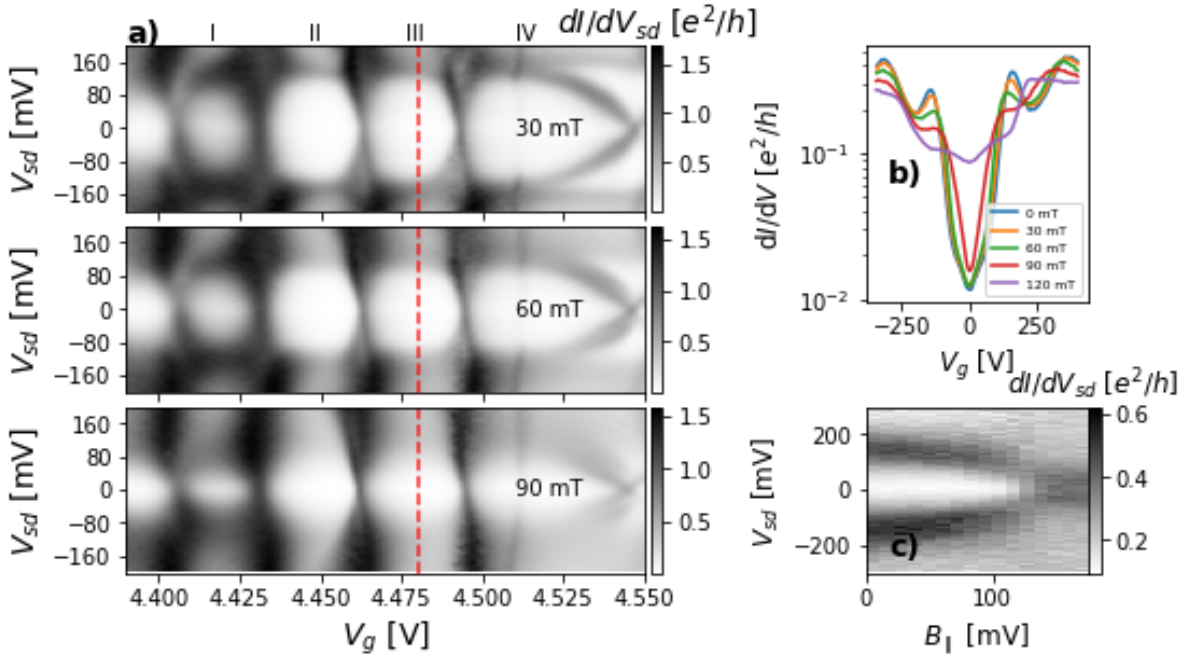

Figure 20: In **a)** stability diagrams of device 2A. The induced superconducting gap and its dependence on the magnetic field applied along the nanowire growth direction is seen. In **b)** $\mathrm{d}I/\mathrm{d}V_{sd}$ of sweeps along the dashed lines in **a)**. The device show sub-gap conductance suppression by a factor of up to ≈40. In **c)** the evolution of the induced gap with B-field as variable. Here $B_{\parallel,c}$ is found to be ≈140 mT for magnetic fields applied along the growth direction of the wire.

Noticing the increase in Γ_S and the YSR-state in Figure 20 the region right next to it in gate was probed. This is seen in Figure 21. Here the first orbital is the same singlet YSR ground state at the end of Figure 20. The distinction between odd and even charge occupation is clear, and Zeeman splitting is seen for doublet excitation lines. The shapes of the excitation lines in V and VI are indicative of them coupling to a state beyond what is considered in a S-QD system. We likely see this additional state entering the gap from both sides, centered around V. This additional state might be due to the presence of a second quantum dot in the system. As a final remark here it appears as if the broadening of the sub-gap states increases with gate bias, which is indicative of increased tunnel broadening from increased lead coupling.

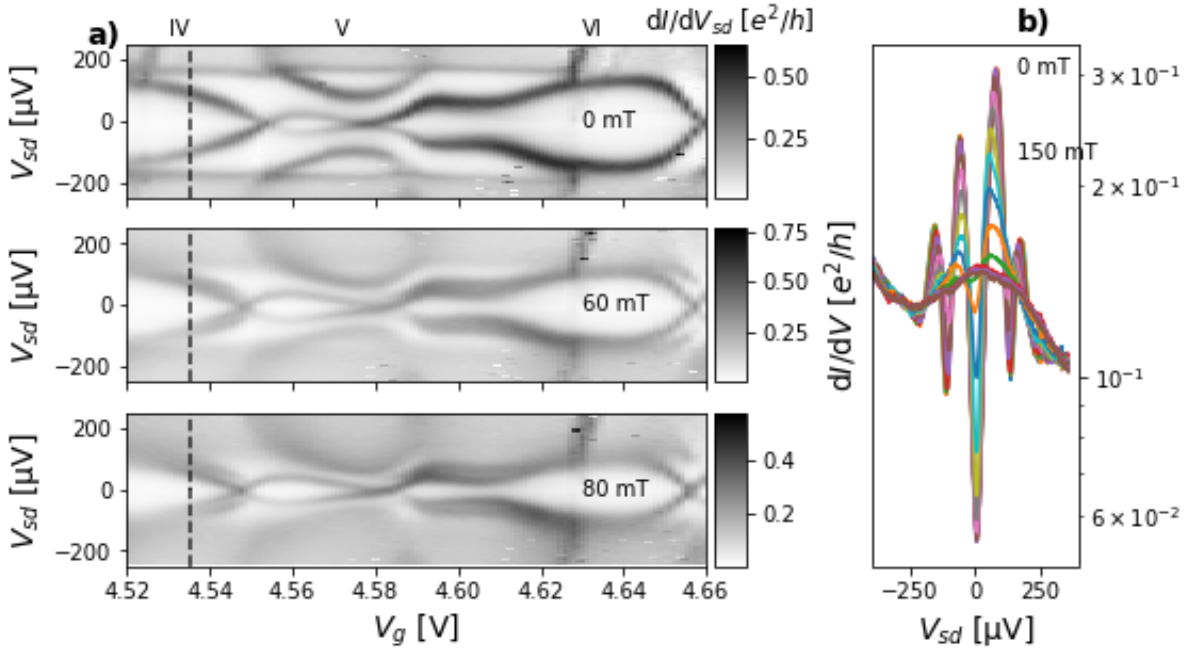

Figure 21: In a) differential conductance, $\mathrm{d}I/\mathrm{d}V_{sd}$, which shows sub-gap states and their evolution with an applied magnetic field. Listing ground states from IV to VI we find a singlet, doublet and singlet. The doublet and second singlet appear to couple to an additional state, which may be from an additional quantum dot present in the system. Note the clear Zeeman splitting of the excitation lines of the rightmost state. Zeeman splitting is also seen for the IV doublet excitation, with a significantly smaller g^*-factor. In b) differential conductance along the dashed line in a) for $B_{\|}$ in the range 0 to 150 mT.

A line-sweep along the dashed line in Figure 21a) is seen in Figure 21b). This measurement was taken as to see how the sub-gap state move in response to the approaching gap and increasing magnetic field. We see how the peaks remain fairly locked in position with increasing magnetic field until they start to avoid the gap. Similar behavior has been seen in e.g [5].

When further increasing V_g a rather noisy, tunnel broadened and uninteresting region was found, which remained so until $V_g \approx$5.66 V. Here instead a region of impeccably sharp features appeared, as seen in Figure 22. Here we see examples of a single dot coupled to a superconductor, with $U > \Delta$ and $\Gamma_S < \Delta$. A comparatively low Γ_S and Γ_N is argued as broadening of the visible sub-gaps is low compared to the size of the gap. We operate in a YSR-regime, as every other orbital has sub-gap states where the spin-degeneracy of the excitation lines are lifted via the Zeeman effect. The orbitals with splitting components have doublet excitation lines.

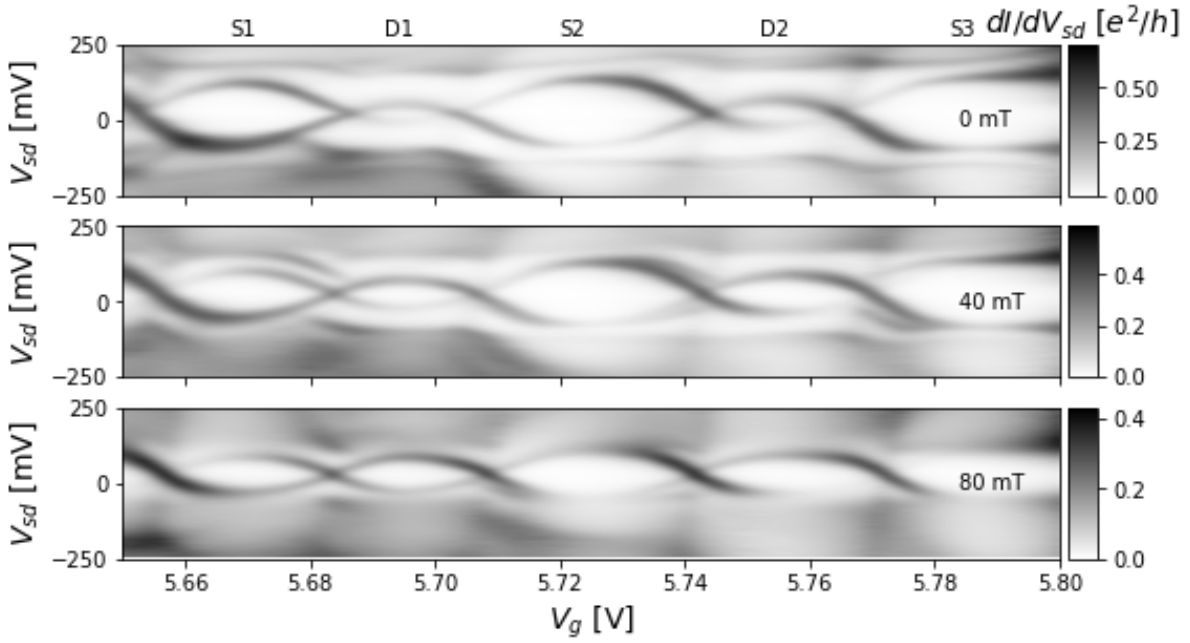

Figure 22: Differential conductance $\mathrm{d}I/\mathrm{d}V_{sd}$ which show sub-gap states and their evolution with applied magnetic field. Transitions between singlet- (S1, S2) to doublet- (D1, D2) ground states are seen. The doublet states split with increasing magnetic field, and an-isotropic dot orbitals result in varying g^*-factors.

We now present device 2B, which is seen in Figure 23. This device operated in a similar regime as 2A, and had a Al-WZ-ZB-Au configuration.

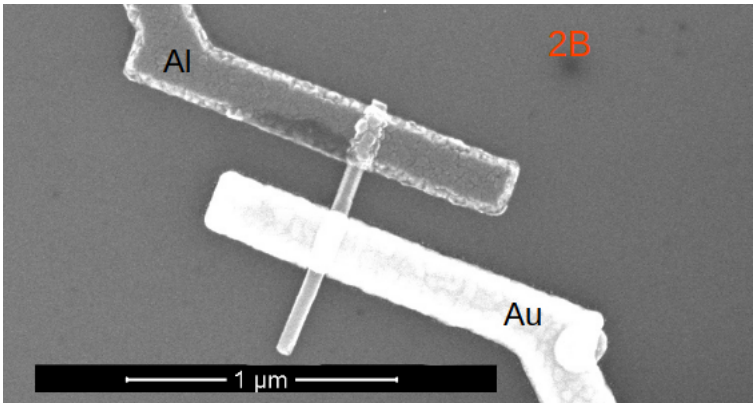

Figure 23: SEM micrograph of device 2B.

In Figure 24 the differential conductance $\mathrm{d}I/\mathrm{d}V_{sd}$ of device 2B in a particularly interesting regime is seen. Dot states with odd occupation are marked in the figure as I, II, III and IV. All of these states have a large Γ_S, and states I, II, IV all are very close to undergo a phase transition from doublet to singlet ground states, while state III looks to have transitioned to a singlet already. The evolution of charge states I and II remain in a doublet ground state with increasing magnetic field, which is not particularly noteworthy. What is slightly remarkable is how stable the excitation lines are in energy. Typically

the excitation lines of a doublet ground state is pushed towards the gap with increasing magnetic field, compare to the evolution of similar charge states in Figure 22.

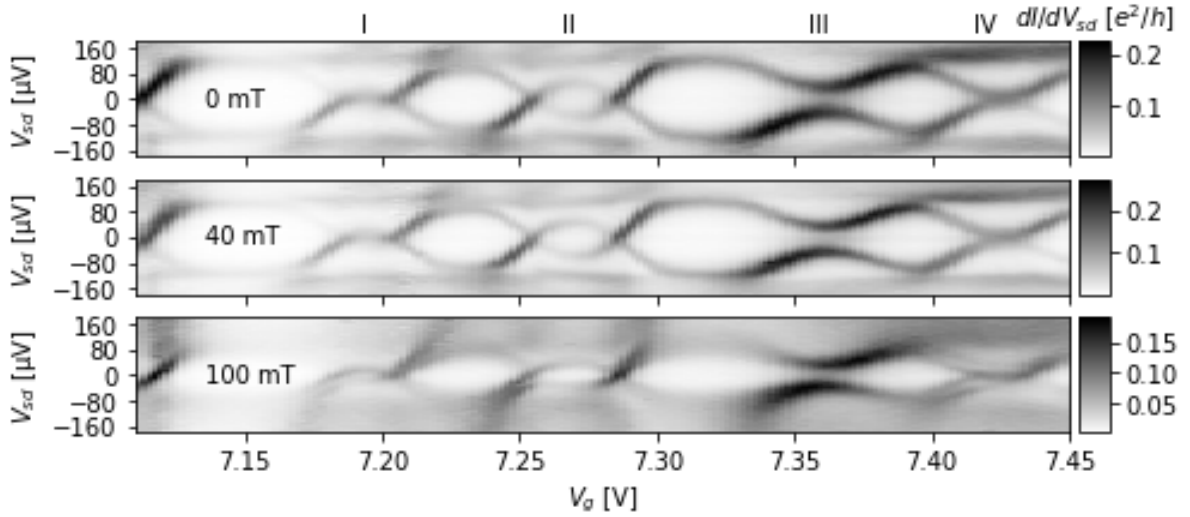

Figure 24: Differential conductance $\mathrm{d}I/\mathrm{d}V_{sd}$ of device 2B in a regime with large Γ_S. Charge states with a local spin of $\pm\frac{1}{2}$ are marked with roman numerals I, II, III and IV.

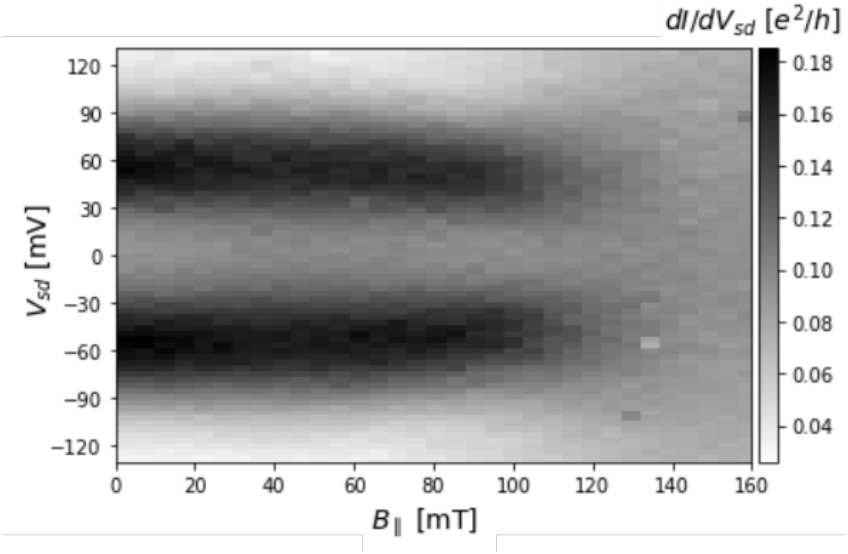

Figure 25: Evolution of excitation lines of a singlet ground state (marked III in Figure 24) with magnetic field. Note how no splitting is seen for the doublet excitation lines.

For states shown here the g^* factor ranges from ≈ 3.2 to 3.8. These comparatively low values are likely part reason as to why the excitation lines seemingly remain stationary. Considering state IV we see that state IV started in a singlet ground state. With increasing magnetic field, a phase transition is induced via the Zeeman effect. The split state moving towards the Fermi level seem to stick to the Fermi level. Meanwhile, state III

does not show any discernable splitting with the magnetic field, which is rather interesting. The excitation lines do get broader to the point where splitting would likely not be resolvable, but it does not broaden significantly at the center of III. Hence, it was deemed interesting to do a linescan at the center of III, with higher resolution in both V_{sd} and $B_{\parallel}$. The result is seen in Figure 25. Here we see that the excitation lines neither broaden nor move in energy until they begin to avoid the incoming gap above $B_{\parallel} > 110$ mT. Likely the region here has a strong coupling to both the superconducting and normal lead, as the singlet ground state and broad excitation lines indicate. Even a low coupling to the normal lead has been theorized to strongly affect the doublet-singlet phase diagram[31], and the large Γ_N may contribute to locking the excitation lines in place.

Moving towards increasingly larger gate biases another interesting region was found, see Figure 26. Here Γ_S is likely comparable to those found in Figure 24, with doublet ground states with a very low doublet to singlet barrier. Charge states labeled II, III show clear quantum phase transitions and were both studied with greater resolution in both V_{sd} and $B_{\parallel}$, see Figure 27.

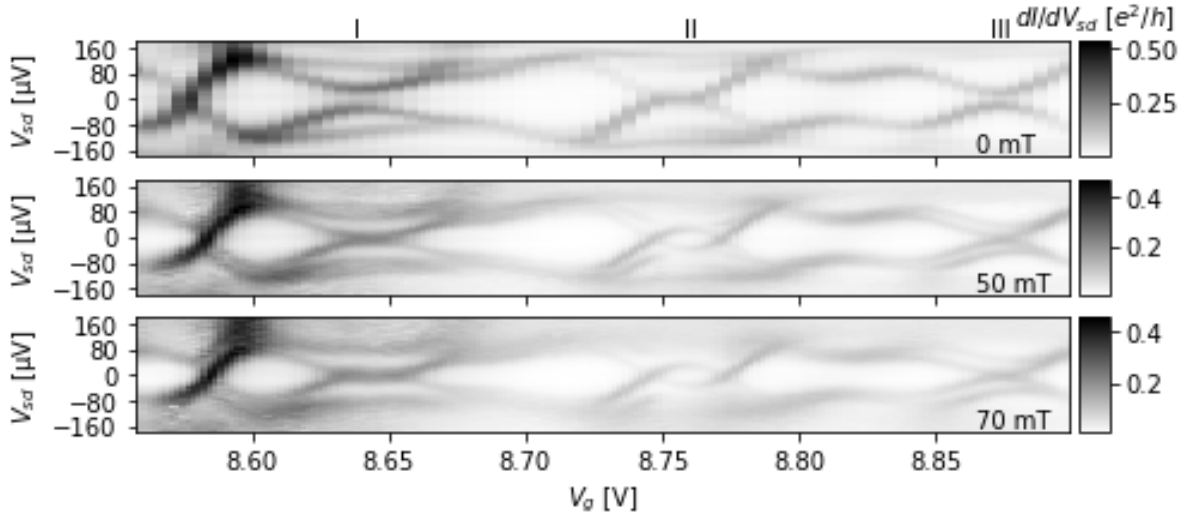

Figure 26: Differential conductance $\mathrm{d}I/\mathrm{d}V_{sd}$ of device 2B across three quantum dot orbitals, marked I-III. In orbitals marked I and III we see quantum phase transitions induced by applied magnetic field.

In retrospect, the charge state labeled I in Figure 26 should have been probed more carefully. The evolution of the excitation lines with the applied magnetic field is very interesting. During the measurements, it was assumed that the evolution of state I was near identical to that of state III, where Γ_S is large enough to induce a YSR-singlet with doublet excitation lines. When the magnetic field is increased the spin-degeneracy is lifted and eventually one of the excitation lines crosses the Fermi level. This might be the case but would require some very large g^* factors to be true. The reason for the newly spawned interest is the additional excitation line at zero magnetic field for I, which are not present for state III. The additional excitation line at 0 magnetic field was during the measurements assumed to be the edge of the gap climbing unusually far down, and not a sub-gap state, which was deemed rather uninteresting at the time. When studied

in greater detail post measurements, the additional excitation line appears to split at 50 mT. The conundrum is whether the additional excitation line actually splits, or if what we are seeing is a more standard doublet excitation with a large enough g^*-factor that one of the split lines is close to escaping the gap at 50 mT. The latter case would require a g^* of almost 16, which would require orbital contributions far beyond what we have observed for the remainder of the sample.

If the additional excitation line does split it is possible that we are observing the first experimental observation of a triplet state, the excited state of a YSR-doublet ground state. The triplet excitation state is predicted to exist in systems with two quantum dots which couple both to each other, and to a superconducting lead. Such a system was studied in [6], where an S-QD-QD-N device was studied in an experimental setting with results aided from a theoretical model. A triplet state was predicted in their simulations, but they failed to observe it in experiments. They attributed the lack of a triplet state in their experiments to the predicted low spectral weight of the triplet state, but also added that the state may be observed in future devices with different fabrication protocols.

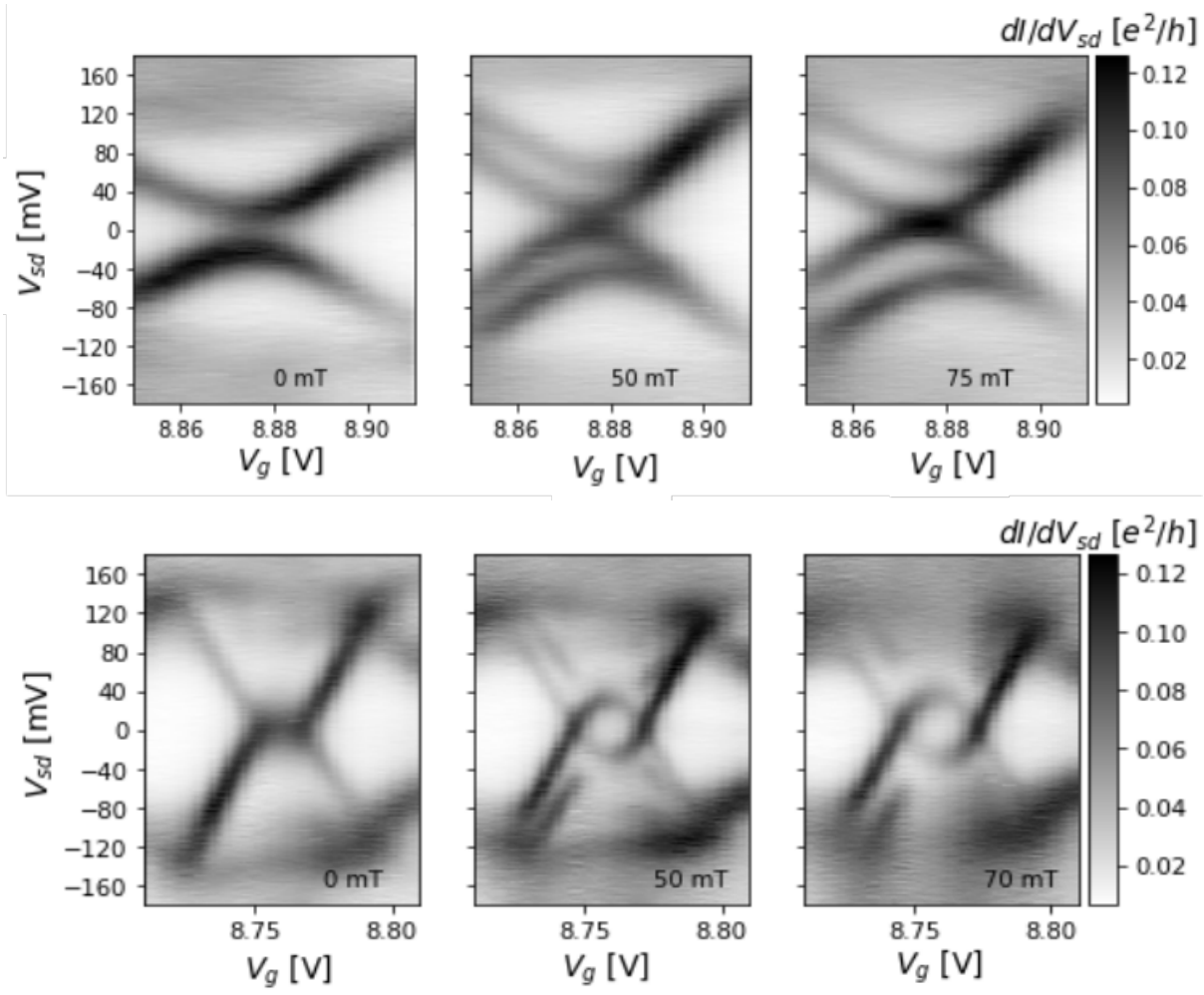

Figure 27: Quantum phase transitions of proximitized quantum dot states. Top row: doublet excitation lines split with applied magnetic field. At high enough B we see that one of the split doublet lines is pushed to zero energy. Bottom row: starting in what might be a singlet ground state, we find a doublet ground state when a magnetic field is applied.

Returning to states II and III, we see these depicted in greater resolution in Figure 27. State III has a doublet excitation at zero magnetic field, which splits with increasing magnetic field. Eventually, one of the splits reaches zero energy and is locked in place. State II appears to have a singlet excitation line, which moves towards the gap with increasing magnetic field.

Finally we present the third device, labeled 2C. This time we have a Au-WZ-ZB-Al configuration, and a SEM micrograph is seen in Figure 28.

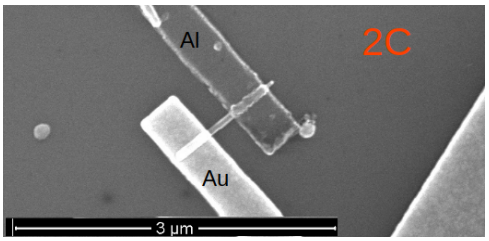

Figure 28: SEM micrograph of device 2C.

This device showed very strong coupling to the superconducting lead, showing only singlet ground states across a wide range of V_g, see Figure 29. Quite possibly this device has two quantum dots in parallel, as there are two overlapping wave-like patterns seen in Figure 29. Each individual wave would then follow the filling of electrons on each dot, and the large Γ_S result in the screening of local half-spins, forcing the phase-transition of doublet ground states to YSR-singlets.

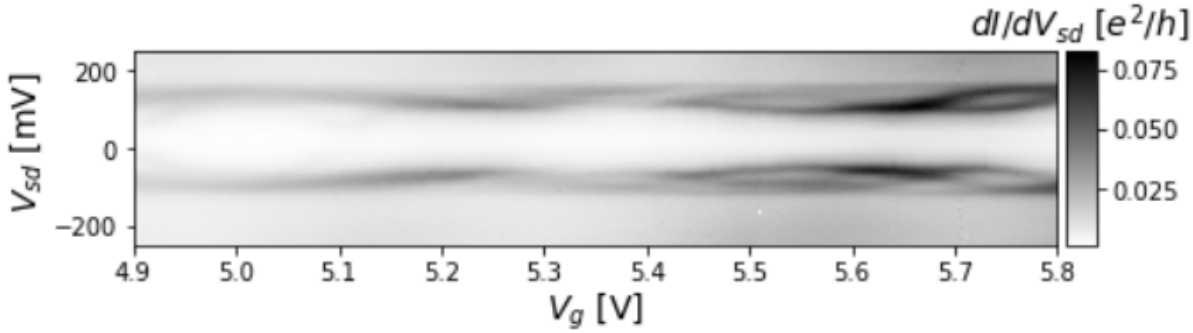

Figure 29: Differential conductance of device 2C. Quantum dot behavior is seen. The device only show singlet ground states, indicative of very large Γ_S.

The sub-gap features are not significantly broadened, so likely the normal lead is only weakly coupled. Still, there is no trace of resonant peaks outside the gap, where one would expect to see Coulomb diamonds. Likely this is caused entirely via tunnel broadening from the superconducting lead. No Zeeman splitting could be observed with the applied magnetic field, the only noticeable effect of applying a magnetic field was line broadening and a shrinking gap. As such the parameter space of this device was rather limited. Still, the device proved interesting, showing not only what can be expected for very large Γ_S, but also providing possibly important clues as to how the QDs are actually formed.

Now we discuss devices 2A-2C, considering information gathered from all devices presented in this thesis. The QD behavior was not planned for any of the devices and it

has not been determined exactly how the QDs actually form. My theory is that Schottky barriers have formed at both the normal and superconducting lead, and the different contacts differ mainly from varying degrees of air exposure. For all devices studied, including devices 1A and 1B presented in Section 4.1, the Ti/Al on ZB contacts indicate lower barriers than those with Ti/Al on WZ. For 1A and 1B no indication of the formation of Schottky barriers could be found at all, these contacts were very transparent. For 2C we found very strong coupling to the superconducting lead, which should translate directly to a low, or very thin, barrier. The discrepancy between 1A,B and 2C can likely be explained sufficiently with increased oxidation on the 2C Ti/Al contact; the spectroscopy devices were all exposed to air for much longer than the Josephson junction devices. The increased exposure was not planned but a consequence of equipment malfunction. This is likely sufficient to explain the difference between the Ti/Al on ZB contacts.

The follow up question is what is different for Ti/Al on WZ, if there is any difference. Devices where this was the case, 2A, and 2B, did not show the same degree of proximitization. My picture here is that the lower electron density of the WZ segments leads to a longer depletion region, i.e thicker barriers, as compared to Ti/Al on ZB. Such a development could explain why the Ti/Al on WZ leads to lower degrees of proximitization than Ti/Al on ZB.

We do know that the Ti/Au contacts have been exposed to air much longer than the Ti/Al contacts, as the Ti/Au contacts were made first. A full fabrication run would likely lead to an additional 9 h (approximately) exposure to air for these contacts. If the culprit is the oxidation of Ti, this could explain the formation of stronger barriers, and whether they are Schottky barriers or not is irrelevant for this argument.

Regarding the possible formation of multiple dots in the system, the discussion is more complicated. Possible causes could be crystal-phase variations that have been unaccounted for, thereby introducing additional barriers in the junction, or band bending effects where the offset caused of a single ZB-WZ interface acts as a barrier between two reservoirs in this case.

5 Conclusion and outlook

The main goal of this project work was to assess the viability of using a HCl wet etch technique for the study of sub-gap states in Al-InAs devices, i.e superconductor-semiconductor hybrids, based on InAs nanowires. With the goal of quantifying contact parameters, Josephson junction devices were fabricated. These devices showed a mix of results, some bad in terms of Josephson junction quality, but also some very good in terms of contact transparency. Based on these results alone the conclusion would have been that these contacts would be very promising for doing spectroscopy on sub-gap states. Even so another experiment was done, with the primary goal of studying e.g the hardness of the gap in a proximitized segment of InAs, and the effect of incorporating a ZB-WZ interface in the junction.

Instead, the devices in this second experiment showed dominant QD behavior. The normal leads in these devices all seemed to be weakly coupled and there were no complications with using them as tunneling probes for the density of states in the proximitized segments. They all showed the same thing: sub-gap states realized by a quantum dot proximitized by a superconductor. Having observed some very clear sub-gap states it's fair to say that the contacts are, at least in some regards, suitable for the studying sub-gap states in superconductor-semiconductor hybrid devices.

If our conjecture on the quantum dots forming due to Schottky barriers and oxidation is correct there are likely issues with reproducibility: does one leave their contacts exposed to air for 5 or 15 hours? Is the ambient air the same in all research facilities all over the world? These issues do not necessarily imply that these contacts should be avoided, but perhaps an experiment should not rely on the barriers introduced by them, although there are interesting bonuses associated with doing so. If either lead couples too strongly one could extract it from the fridge, leave it in ambient air for a few hours to oxidize, and then cool it down again. A slightly simpler approach than creating an entirely new batch of devices.

Rather using the contacts with the goal of minimizing oxidation is the safer option. The oxidation of the normal lead is likely unavoidable but is also not much of a concern. We want low coupling to the normal lead in spectroscopy measurements. Thicker contacts would likely oxidize slower, but one misses out on the much-desired increase in the critical field. This is of course not a problem for the normal contact, and in retrospect using thicker contacts for the normal lead is an obvious choice. In combination with barriers formed either via electrostatic plunger gates or via crystal-phase variations the contacts used in this project should serve the purpose of studying superconductor-semiconductor hybrids well.

A typical conclusion reached when using aluminum as a superconducting lead in superconductor-semiconductor hybrids is that the critical field is too low. Likely they are in general correct, and changing to e.g vanadium, might solve this problem for them. Still, fabrication techniques and contact designs reducing contact dimensions remain valid options. In this project, the critical field was increased by over 40% with very minor changes in design. Possibly one could use a design utilizing evaporated Ti/Au (or the normal metal of one's choosing) as "ramps" on the superconducting lead side, leaving enough space to still allow for Ti/Al to be deposited on the nanowire directly. As the Ti/Au is likely deposited first this is not much of an increase in fabrication difficulty, but

might allow for thinner Ti/Al contacts to be used.

During this project, I could not find any material where it had been studied how hybridized sub-gap states evolve as a function of temperature, the occasional numerical simulation, but no experiments. This is not particularly surprising, likely the results are rather uninteresting and also would not present an ideal ground for further research. Even more so it would be very difficult to study, adding thermal broadening on top of the already present tunnel broadening would result in significant line-broadening. Even so, it piqued my interest as the temperature is the only other easily accessible parameter we can use to alter the size of the superconducting gap, apart from magnetic fields. Hence, what follows are suggestions on what could be investigated using temperature as an experimental variable.

In several of the studied articles, and presented as part of this thesis, is the case where the Zeeman effect pushes a sub-gap excitation in a linear fashion until it approaches the incoming gap, at which point it starts to avoid the gap. This regime might be possible to study using a combination of magnetic fields and temperature variations. Using a superconductor with low critical temperature, but with long coherence length would be ideal for a study in this regime. A suitable candidate might be titanium, with a coherence length and critical field comparable to aluminum, but with a critical temperature of 0.4 K instead of 1.2 K.

Another topic for studies involving temperature as variable may be an investigation on the impact of spin screening from electrons from the normal lead. It has been suggested that even very low coupling strengths to the normal lead may have a large impact on the singlet-doublet phase-diagram[31]. It has also been suggested that this could be studied using barriers defined with plunger gates, similar to what was done in e.g [5]. However, the use of plunger gates effectively enforces the use of larger dots, which prohibits using superconducting leads with large Δ for the study. Likely Al is the sole candidate, albeit a very strong one. But even considering these limitations it may be possible to study the impact factor from normal screening electrons in such devices, with the added caveat that one changes the coupling strength to the tunneling probe during the experiment.

A different approach would be to use systems with spatially well-defined barriers, e.g those introduced from crystal-phase variations, and instead vary the temperature. Tuning the temperature varies the number of normal electrons available for screening in accordance with Boltzmann statistics, while barrier strengths should remain largely constant for small variations in temperature. Simultaneously, the screening from Bogoliubov quasiparticles increases through the same means, but this contribution could likely be minimized by choosing a large gap superconductor. This system would allow for very small dots with large charging energies, leaving a lot of freedom for choosing the superconducting lead. It is also possible to design devices with a strong barrier to the normal lead, which ought to be done as a precaution for maintaining a stable tunneling probe throughout the experiment. The suggested experimental setup may present a close to ideal setting for studying the impact of the screening from normal electrons on the singlet-doublet phase-diagram.

In this thesis we studied systems where a single quantum dot is coupled to a superconductor. A natural extension is to study a quantum dot molecule coupled to a superconductor. This is essentially what was done in [3], in a S-QD-QD-N system with dots were connected in *series*. However, there are advantages to studying charge and

spin transport in systems with *parallel* quantum dots, as discussed in [32]. The parallel dots studied in [32] were formed using electrodes as side-gates on a quantum dot, with the dot formed via crystal-phase engineered barriers in InAs nanowires. The side-gates allow for the orbitals in each dot to be controlled separately. The extension from work done for this thesis, to studying proximitized parallel quantum dots is straight-forward; simply equip devices similar to the spectroscopy devices fabricated in this thesis with side-gates. The main crux is likely to be decide wether to use a crystal-phase engineered barrier for the superconducting lead, or attempt to use one formed by oxidation. The first option is tried in N-DQD-N devices in [32], but they had significantly less rigid demands on transparent contacts. The second option is partly what is presented in this thesis. Barriers introduced using an oxidation approach can likely be positioned very flexibly on the wire, but may prove difficult to reliably reproduce.

There is plenty of interesting physics to study in relation to superconductor-semiconductor hybrids. We conclude that the fabrication requirements mentioned in other work have likely been exaggerated. It was shown in this project that a very weak HCl-acid could be used to process high quality superconductor contacts, more than capable of reproducing the results of a wide range of published work.

References

[1] C. W. J. Beenakker, "Quantum transport in semiconductor-superconductor microjunctions," jun 1994.

[2] L. Hofstetter, S. Csonka, J. Nygård, and C. Schönenberger, "Cooper pair splitter realized in a two-quantum-dot Y-junction," *Nature*, vol. 461, pp. 960–963, oct 2009.

[3] C. Jünger, A. Baumgartner, R. Delagrange, D. Chevallier, S. Lehmann, M. Nilsson, K. A. Dick, C. Thelander, and C. Schönenberger, "Spectroscopy of the superconducting proximity effect in nanowires using integrated quantum dots," *Communications Physics*, vol. 2, p. 76, dec 2019.

[4] M. Leijnse and K. Flensberg, "Introduction to topological superconductivity and Majorana fermions," *Semiconductor Science and Technology*, vol. 27, p. 124003, dec 2012.

[5] A. Jellinggaard, K. Grove-Rasmussen, M. H. Madsen, and J. Nygård, "Tuning Yu-Shiba-Rusinov states in a quantum dot," *Physical Review B*, vol. 94, p. 064520, aug 2016.

[6] K. Grove-Rasmussen, G. Steffensen, A. Jellinggaard, M. H. Madsen, R. Žitko, J. Paaske, and J. Nygård, "Yu-Shiba-Rusinov screening of spins in double quantum dots," *Nature Communications*, vol. 9, pp. 1–6, dec 2018.

[7] M. Nilsson, L. Namazi, S. Lehmann, M. Leijnse, K. A. Dick, and C. Thelander, "Single-electron transport in InAs nanowire quantum dots formed by crystal phase engineering," *Physical Review B*, vol. 93, no. 19, pp. 1–7, 2016.

[8] O. Penrose and L. Onsager, "Bose-einstein condensation and liquid helium," *Physical Review*, 1956.

[9] J. Bardeen, L. N. Cooper, and J. R. Schrieffer, "Theory of superconductivity," *Physical Review*, vol. 108, pp. 1175–1204, dec 1957.

[10] J. F and J. Annett, *Superconductivity, Superfluids and Condensates*. Oxford Master Series in Physics, OUP Oxford, 2004.

[11] L. N. Cooper, "Bound electron pairs in a degenerate fermi gas [1]," nov 1956.

[12] E. Maxwell, "Isotope Effect in the Superconductivity of Mercury," *Physical Review*, vol. 78, pp. 477–477, may 1950.

[13] A. Barone and G. Paternò, *Physics and Applications of the Josephson Effect*. Wiley, jul 1982.

[14] H. A. Nilsson, P. Samuelsson, P. Caroff, and H. Q. Xu, "Supercurrent and Multiple Andreev Reflections in an InSb Nanowire Josephson Junction," *Nano Letters*, vol. 12, pp. 228–233, jan 2012.

[15] Y. Makhlin, G. Schön, and A. Shnirman, "Quantum-state engineering with Josephson-junction devices," *Reviews of Modern Physics*, vol. 73, pp. 357–400, apr 2001.

[16] N. F. Pedersen, O. H. Soerensen, J. Mygind, P. E. Lindelof, M. T. Levinsen, and T. D. Clark, "Direct detection of the Josephson radiation emitted from superconducting thin-film microbridges," *Applied Physics Letters*, vol. 28, no. 9, pp. 562–564, 1976.

[17] A. H. Silver, A. B. Chase, M. McColl, and M. F. Millea, "Superconductor-semiconductor device research," in *AIP Conference Proceedings*, vol. 44, pp. 364–379, AIP, 1978.

[18] J. A. Sauls, "Andreev Bound States and Their Signatures," may 2018.

[19] D. V. Averin and K. K. Likharev, "Coulomb blockade of single-electron tunneling, and coherent oscillations in small tunnel junctions," *Journal of Low Temperature Physics*, vol. 62, pp. 345–373, feb 1986.

[20] E. J. Lee, X. Jiang, M. Houzet, R. Aguado, C. M. Lieber, and S. De Franceschi, "Spin-resolved Andreev levels and parity crossings in hybrid superconductor-semiconductor nanostructures," *Nature Nanotechnology*, vol. 9, pp. 79–84, dec 2014.

[21] T. Meng, S. Florens, and P. Simon, "Self-consistent description of andreev bound states in josephson quantum dot devices," *Physical Review B*, vol. 79, Jun 2009.

[22] H. Courtois, M. Meschke, J. T. Peltonen, and J. P. Pekola, "Origin of Hysteresis in a Proximity Josephson Junction," *Physical Review Letters*, vol. 101, p. 067002, aug 2008.

[23] K. Gharavi, G. W. Holloway, R. R. LaPierre, and J. Baugh, "Nb/InAs nanowire proximity junctions from Josephson to quantum dot regimes," *Nanotechnology*, vol. 28, jan 2017.

[24] T. Nishio, T. Kozakai, S. Amaha, M. Larsson, H. A. Nilsson, H. Q. Xu, G. Zhang, K. Tateno, H. Takayanagi, and K. Ishibashi, "Supercurrent through InAs nanowires with highly transparent superconducting contacts," *Nanotechnology*, vol. 22, p. 445701, nov 2011.

[25] H. Zhang, Ö. Gül, S. Conesa-Boj, M. P. Nowak, M. Wimmer, K. Zuo, V. Mourik, F. K. De Vries, J. Van Veen, M. W. De Moor, J. D. Bommer, D. J. Van Woerkom, D. Car, S. R. Plissard, E. P. Bakkers, M. Quintero-Pérez, M. C. Cassidy, S. Koelling, S. Goswami, K. Watanabe, T. Taniguchi, and L. P. Kouwenhoven, "Ballistic superconductivity in semiconductor nanowires," *Nature Communications*, vol. 8, pp. 1–7, jul 2017.

[26] Y. J. Doh, J. A. Van Dam, A. L. Roest, E. P. Bakkers, L. P. Kouwenhoven, and S. De Franceschi, "Applied physics: Tunable supercurrent through semiconductor nanowires," *Science*, vol. 309, pp. 272–275, jul 2005.

[27] S. Abay, H. Nilsson, F. Wu, H. Q. Xu, C. M. Wilson, and P. Delsing, "High critical-current superconductor-InAs nanowire-superconductor junctions," *Nano Letters*, vol. 12, pp. 5622–5625, nov 2012.

[28] H. I. Jørgensen, K. Grove-Rasmussen, T. Novotný, K. Flensberg, and P. E. Lindelof, "Electron transport in single-wall carbon nanotube weak links in the fabry-perot regime," *Physical Review Letters*, vol. 96, p. 207003, may 2006.

[29] G. Niebler, G. Cuniberti, and T. Novotný, "Analytical calculation of the excess current in the Octavio–Tinkham–Blonder–Klapwijk theory," *Superconductor Science and Technology*, vol. 22, p. 085016, jul 2009.

[30] W. Chang, S. M. Albrecht, T. S. Jespersen, F. Kuemmeth, P. Krogstrup, J. Nygård, and C. M. Marcus, "Hard gap in epitaxial semiconductor-superconductor nanowires," *Nature Nanotechnology*, vol. 10, pp. 232–236, mar 2015.

[31] R. Žitko, J. S. Lim, R. López, and R. Aguado, "Shiba states and zero-bias anomalies in the hybrid normal-superconductor Anderson model," *Physical Review B - Condensed Matter and Materials Physics*, vol. 91, p. 045441, jan 2015.

[32] M. Nilsson, *Charge and Spin Transport in Parallel-Coupled Quantum Dots in Nanowires*. PhD thesis, Lund University, 2018.